

PREFERENTIALLY ORIENTED GROWTH OF DIAMOND FILM ON SILICON  
SUBSTRATE

by

Anupam K.C., B.S.

A thesis submitted to the Graduate Council of  
Texas State University in partial fulfillment  
of the requirements for the degree of  
Master of Science  
with a Major in Material Physics  
August 2019

Committee Members:

Edwin L. Piner, Chair

Luisa Scolfaro

Wilhelmus Geerts

**COPYRIGHT**

by

Anupam K.C.

2019

## **FAIR USE AND AUTHOR'S PERMISSION STATEMENT**

### **Fair Use**

This work is protected by the Copyright Laws of the United States (Public Law 94-553, section 107). Consistent with fair use as defined in the Copyright Laws, brief quotations from this material are allowed with proper acknowledgment. Use of this material for financial gain without the author's express written permission is not allowed.

### **Duplication Permission**

As the copyright holder of this work I, Anupam K.C., authorize duplication of this work, in whole or in part, for educational or scholarly purposes only.

## **ACKNOWLEDGMENT**

I am very fortunate to have had the opportunity to work and grow alongside many fine individuals throughout my graduate experience in M.S. in Materials Physics at Texas State University. I would like to thank my advisor Dr. Edwin Piner for his dedication and personal investment in his students and his graceful abilities to teach and motivate. I would also like to thank my committee members Dr. Luisa Scolfaro and Dr. Wilhelmus Geerts for their guidance and patience. I would like to thank Anwar Siddique for his substantial contributions to the diamond growth and technical support. I would like to thank Texas State's ARSC and NRSC technical teams and support staff with special acknowledgment to Dr. Casey Smith, Alissa Savage, Joyce Anderson, and Dr. Dmitri Lyashenko for the many hours spent training and answering my questions. I would like to thank the National Science Foundation (NSF) for providing me with financial support for my thesis. I am extraordinarily grateful for my family, which encompasses a list of exceptional individuals too long to enumerate and too important to describe. Their continual encouragement and unconditional support throughout my work are invaluable.

## TABLE OF CONTENTS

	<b>Page</b>
ACKNOWLEDGMENT.....	iv
LIST OF TABLES .....	vii
LIST OF FIGURES .....	viii
ABSTRACT.....	xiii
CHAPTER	
I. INTRODUCTION .....	1
II. BACKGROUND .....	3
2.1. Diamond and its properties .....	3
2.2. Nucleation and growth of thin films .....	5
2.3. Growth of coalescent films .....	6
2.4. Thin Film deposition techniques.....	9
2.5. Stress development during thin film deposition .....	12
2.5.1. Epitaxial stress .....	12
2.5.2. Intrinsic stress .....	13
2.5.3. Surface stress effect .....	15
2.5.4. Stress generation due to coalescence of grains boundaries .....	16
2.5.5. Thermal stress .....	16
2.6. Diffusion of Nickel on Silicon substrate during annealing.....	17
2.7. Texture development in thin films.....	19
2.8. Nucleation and growth of diamond film.....	20
2.8.1. Diamond nucleation .....	20
2.8.2. Diamond growth .....	22
2.9. Texture Development in CVD Diamond.....	25
3.0. Heteroepitaxial growth of diamond films on a nickel substrate .....	27
3.1. Characterization techniques .....	28
3.1.1. Scanning Electron Microscope .....	28
3.1.2. Atomic force microscopy.....	31

3.1.3. X-ray diffraction .....	33
3.1.4. Raman spectroscopy .....	35
3.1.5. Ellipsometry .....	38
3.1.6. Surface profilometry .....	40
III. EXPERIMENTS .....	42
IV. RESULTS .....	45
4.1. Diamond growth on annealed nickel thin films .....	45
4.1.1. Nickel film characterization.....	45
4.1.2. Nickel nanodots array and distributions .....	47
4.1.3. Phases changes in Nickel thin films by annealing .....	53
4.1.4. Diamond growth and characterization .....	56
4.1.5. Nucleation and growth of diamond film.....	57
4.1.6. Quality of diamond film.....	61
4.2. Diamond growth on nickel modification layer without annealing .....	66
4.2.1. Substrate pre-treatment and diamond deposition.....	66
4.2.2. Characterization .....	66
4.2.3. Diamond nucleation and crystal development.....	67
4.2.4. Enhancement mechanism of diamond films grown on Ni modification layers.....	73
4.2.5. Development of diamond texture.....	76
V. CONCLUSIONS.....	81
5.1. Diamond growth on annealed seeded wafers with nickel layers .....	81
5.2. Diamond growth on Si wafer with nickel modification layers .....	81
5.2.1. High Growth rate /Nucleation.....	81
5.2.2. High-quality diamond film and crystallinity.....	82
5.2.3. Oriented diamond films along (220).....	82
VI. FUTURE WORK.....	83
APPENDIX SECTION.....	84
REFERENCES .....	88

## LIST OF TABLES

<b>Table</b>	<b>Page</b>
1. Parameter range for diamond synthesis by filament HFCVD method .....	22
2. Possible transformation by primary and secondary twinning.....	26
3. Raman peaks for diamond and non-diamond carbon .....	36
4. Thickness and roughness measurements for Ni thin film on Si.....	45
5. The diamond thickness and roughness measured by surface profilometer.....	74
6. Relative intensity of diffracted X-rays beams for random assembly of diamond crystals. ....	76

## LIST OF FIGURES

Figure	Page
1. Ternary phase diagram of carbon allotropes.....	3
2. Face Centered cubic structure of Diamond.....	4
3. Basic Models for thin film growth a) Volmer-Weber Model, b) Frank-Van der Merwe Model, and c) Stranski-Krastanov Model.....	7
4. Types of thin film growth on a polycrystalline film with a) immobile grain boundaries and b) mobile grain boundaries.....	8
5. Angstrom Engineering Evo Vac.....	9
6. Schematic of HFCVD apparatus.....	10
7. Texas State Crystallume CVD system.....	11
8. The variation of growth stress with an increase in the film thickness.....	13
9. Grains of the polycrystalline film before and after coalescence.....	15
10. Nickel Silicide phase changes with different annealing temperature .....	18
11. Ni-Si equilibrium phase diagram .....	19
12. Schematic of the process occurring in CVD diamond.....	23
13. Schematic model for the development of thin film by Van der Drift.....	25

14. The schematic diagram for the main parts of the scanning electron microscope .....	29
15. FEI Helios Nano lab 400 Scanning electron microscope at Texas State.....	30
16. General block diagram of AFM working principle.....	31
17. Bruker atomic force microscope at Texas State.....	32
18. X-rays diffraction .....	33
19. Rigaku Smart Lab X-ray diffraction tool in Texas State.....	35
20. Horiba Lab RAM HR Raman spectroscope at Texas State.....	37
21. The schematic diagram for Ellipsometer set up a) Variable angle spectroscopic tools and b) overhead view of variable angle spectroscopy.....	38
22. J.A. Woollam ellipsometer at Texas State.....	39
23. A schematic diagram of the stylus profilometer measurement set up along length L, with scan axis x, and displacement axis.....	40
24. Dektak XT Surface profilometer at Texas State.....	41
25. Spectroscopic Results for Nickel thin film.....	46
26. Optical constant results for Nickel film from ellipsometer.....	46
27. AFM images (5 $\mu\text{m}$ $\times$ 5 $\mu\text{m}$ ) scan for 5 nm nickel thin film on Silicon.....	47
28. SEM images for Ni nanodots (15 nm Ni film on Si) annealed at, a) 600 $^{\circ}\text{C}$ for 30 min and b) 600 $^{\circ}\text{C}$ for 1 h, in N <sub>2</sub> atmosphere.....	48

29. SEM images for Ni nanodots (15 nm Ni film on Si) annealed at, a) 1000°C for 30 min, and b) 1000°C for 1 h, in N <sub>2</sub> atmosphere.....	49
30. Nickel nanodots density and area distribution with nickel film thickness.....	49
31. Distribution of Ni nanodots on a Si(111) substrate.....	51
32. SEM images for Ni nanodots formed on Si substrate;.....	52
33. XRD analysis of 15 nm Ni film before and after annealing at various temperature.....	54
34. Raman spectrum of 15nm nickel film before and after annealing.....	55
35. SEM images for annealed diamond seeded wafer at (a) 800 °C for 30 min, and (b) 800 °C for 30 min + 920 °C for 1 min.....	56
36. SEM images for diamond (a) ‘cauliflower’ texture in the annealed Ni film on Si (111) for 800 °C for 30 min + 920 °C for 1 min. and (b) diamond seeded growth directly on Si (111).....	58
37. SEM images for 3 h diamond growth on the annealed Ni thin film on Si (111) at 800 °C for 30 min.....	58
38. SEM images of diamond growth on the two-step (3 + 6 h) annealed sample.....	59
39. Medium resolution parallel beam XRD scan for 9 h diamond growth on annealed Ni film on Si (111) at 800 °C for 30 min.....	60

40. Raman spectra for diamond grown on the one-step annealed Ni thin film.....	62
41. Integrated curve fitting, with baseline (red), used to calculate the peak areas for diamond and NDC.....	63
42. AFM images of (a) $5\ \mu\text{m} \times 5\ \mu\text{m}$ and (b) $10\ \mu\text{m} \times 10\ \mu\text{m}$ , of the diamond film at 45 mm from the center of the wafer.....	64
43. SEM images of the diamond surface grown on 15 nm annealed Ni for 9 h at 45 mm from the center of the wafer.....	65
44. Raman spectra for the various samples in this study.....	68
45. SEM images of diamond films grown on nickel modification layers.....	70
46. Non-diamond composition from diamond Raman peaks.....	71
47. Variation of diamond thickness and NDC content with Ni modification layer thickness.....	72
48. AFM images indicating surface morphologies of the diamond films grown with different Ni modification layers (wafer center).....	75
49. Crystal orientation distribution of diamond obtained from XRD for the samples grown with varied Ni modifications layer thickness .....	78
50. Medium resolution parallel beam XRD scans for diamond growth on different Ni modification layer thickness.....	79

## LIST OF ABBREVIATIONS

<b>Abbreviation</b>	<b>Description</b>
GaN	Gallium Nitride
HFCVD	Hot Filament Chemical Vapor Deposition
CVD	Chemical Vapor Deposition
HEMT	High Electron Mobility Transistor
TBR	Thermal Boundary Resistance
MPCVD	Microwave Plasma Chemical Vapor Deposition
AFM	Atomic Force Microscope
SEM	Scanning Electron Microscope
RMS	Root mean Square
XRD	X-ray diffraction
EDS	Electron Dispersion Spectroscopy
RPM	Rotations per minute
sccm	Standard cubic centimeters per minute
psi	Pounds per square inch
NDC	Non-Diamond Carbon

## **ABSTRACT**

A multistep deposition technique has been developed to grow and nucleate a diamond film directly on Silicon substrate in a hot filament chemical vapor deposition system. The high-quality diamond film is deposited on the silicon substrate with an intermediate nickel thin film with less graphitic co-deposition. The extremely high surface energies, interfacial lattice misfit and strain energies between the diamond film and the non-diamond substrate is the main problems for the oriented film on the substrate. Thus, an intermediate thin nickel film is deposited on the silicon substrate to develop the texture and the oriented diamond film by the process of annealing. The annealing temperature of the film is determined from the molten phase state of the nickel, silicon, carbon, and hydrogen. The growth kinetics and diamond film texture are also studied by the growth of diamond film on different nickel modification layers without annealing. The oriented diamond film is anticipated to have high thermal conductivity and low surface roughness and is useful as a substrate for high electron mobility transistor (HEMT) devices to improve the thermal boundary resistance (TBR). The purpose of this research is to grow an oriented diamond film on a silicon substrate without graphitic interlayers, and the results of this study will be valuable for the semiconductor industry such as the integration of diamond in ultra-high power (GaN/AlGaN) HEMT devices to increase the device lifetime and thermal management.

## I. INTRODUCTION

CVD diamond deposition has been extensively studied by various research groups worldwide since the 1980s [1,2]. The deposition technique involves the deposition of a carbon-containing gas precursor on a solid substrate [1]. The substrate may be either a bulk diamond or non-diamond substance. The deposition of diamond on a non-diamond substrate usually requires an extra nucleation step because the diamond does not typically grow spontaneously on non-diamond materials [1,3]. These steps provide the non-diamond substrate with the necessary diamond seeds that grow three-dimensionally until the grains coalesce, forming a continuous polycrystalline diamond film with the average grains size increasing with increasing films thickness. The resulting films are poly, nano, ultra-crystalline, depending upon the grain size and their macroscopic properties [3].

The purpose of this research is to develop a multistep deposition technique to nucleate and grow oriented diamond film directly on the silicon substrate in a hot filament chemical vapor deposition system. The oriented growth of diamond film on the non-diamond substrate by chemical vapor deposition has long been sought due to its potential applications in the microelectronics industry [4]. High-quality diamond film on the non-diamond substrate is expected to grow without graphitic co-deposition. The extremely high surface energy of diamond ( $5.3-9.2 \text{ J/m}^2$  along the low index planes) and the existence of interfacial misfit and strain energy between the diamond film and non-diamond substrate are believed to be the primary obstacles in forming oriented two-dimension diamond nuclei [5]. For this, a thin intermediate Ni thin film (which has a close lattice parameter match with diamond) is deposited on the silicon substrate to change the strain energy and interfacial energy between the diamond film and silicon

substrate. Nickel has high solubility with carbon, and its strong catalytic effect on hydrocarbon deposition and subsequent graphite formation at low pressure have been expected to prevent CVD diamond nucleation on Si substrate without deposition of intermediate graphitic layer [6]. The diamond seeded wafer on top of nickel modified layers was annealed at different temperatures before diamond growth. The annealing temperature is determined by the expected molten phase based on analysis of the Ni-Si equilibrium phase diagram that would be a liquid layer composed of nickel, silicon, carbon, and perhaps hydrogen [5,6]. The texture formation by diamond nucleation and growth on thin nickel modification layers without annealing is also studied. The oriented diamond film has been achieved by the reorientation of seeded diamond particles into alignment with the nickel film due to the interaction between the diamond and nickel lattices.

In this work, the oriented diamond film with different thickness deposited on a silicon substrate is characterized via X-ray diffraction techniques, Atomic force microscope (AFM), Raman spectroscopy, surface profilometry and Scanning electron microscopy (SEM).

## II. BACKGROUND

### 2.1. Diamond and its properties

The family of Carbon-based materials has grown substantially since the middle of last century. The possible forms of carbon through  $sp^1$ ,  $sp^2$ ,  $sp^3$  hybridization of its valance configuration provides a wide range of possible carbon forms [1]. The most widely accepted equilibrium carbon structures, based on hybridization, originate from the work of Heimann et al. [7]. The first ternary phase diagram is shown in the figure below [7]. The three main vertices of the diagram are defined by the hybridization states, while the interior of the diagram represent the materials processing in a mixture of respective hybridizations.

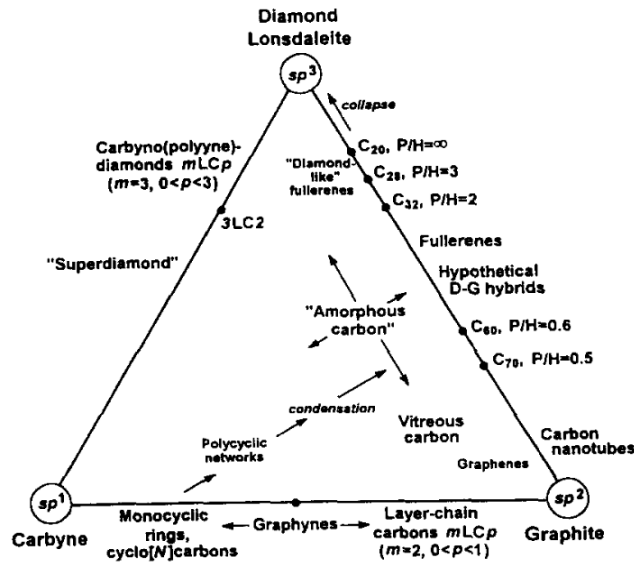
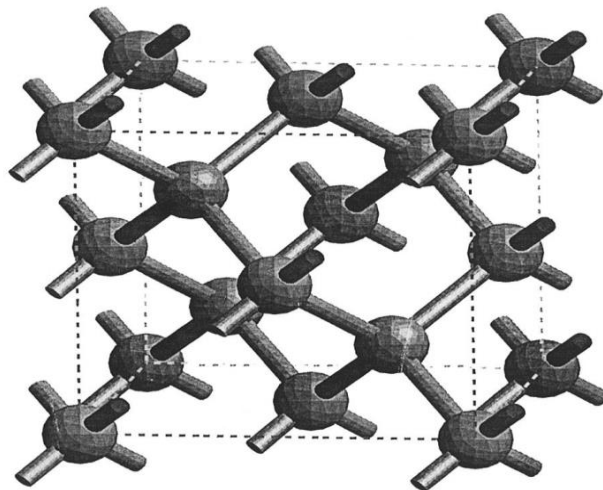


Figure 1. Ternary phase diagram of carbon allotropes [7].

The classification uses  $sp^n$  groups for allotropes owning mixtures of hybridizations. Such groups have ‘n’ hybridization, which is defined as being ( $1 < n < 3$ ;  $n \neq 2$ ). The number of different carbon allotropes is extensive, including the well-known materials; diamond, graphite, graphene, carbon nanotubes, fullerenes, amorphous carbon films, and many others.

The applications of diamond in industry are very well known. At standard temperature and pressure, it is a metastable form of carbon, and as such, it is not formed at the surface of the earth. Graphite is the thermodynamically stable allotrope of carbon at standard temperature and pressure. Their standard enthalpy differs by just 2.9 kJ/mol, but an activation barrier separates the two phases from spontaneous conversion [8]. So, diamond is a metastable form of carbon which is kinetically stable but not thermodynamically. The  $sp^3$  hybridized carbon structure of diamond forms a tetrahedral bonding arrangement which has a face-centered cubic lattice crystal structure, shown in Figure 2.



**Figure 2.** Face Centered cubic structure of Diamond[10].

The carbon atoms forming diamond have a strong covalent bond. The strength of carbon bonding is 347 kJ/mol, and so substantial energy must be enforced to remove a carbon atom which is bonded in the diamond lattice [10]. Highlights of diamond properties include a tightly rigid structure, lowest compressibility due to its large Young's modulus (1220 GPa), highest thermal conductivity at room temperature ( $2 \times 10^3 \text{ W m}^{-1} \text{ K}^{-1}$ ), high resistivity ( $10^{16} \text{ } \Omega\text{-cm}$  at  $20 \text{ } ^\circ\text{C}$ ), wide band gap (5.37 eV), excellent chemical inertness, broad optical transparency (ultraviolet to infrared region) and thermal oxidation resistance [1,8].

The chemical vapor deposition (CVD) process enables cost-effective deposition of diamond for applications in the fields of micromechanical processes in the form of coatings. Examples of such mechanical applications of CVD diamond thin films are diamond coating mechanical tools for soft metals and woods, low wear parts, and biomedical applications [11,12].

## **2.2. Nucleation and growth of thin films**

The regime of film growth determines the quality of the deposited films. Microstructural characteristics of thin films, such as grains size and orientation, determine the films performance and reliability in a great variety of electronic, photonic, and mechanical applications. So, the specific microstructure of these films must be reproducible, and the deposition process must be controllable. At the start of the deposition process, the atoms condense on the substrate surface and undergo several processes such as re-evaporation, nucleation of the cluster, capture by the cluster, etc. [13]. The chemical bond with the surface atoms is formed during the process of condensation, and the surface mobilities of atoms depend upon the strength of the surface

bonds and whether the bond is metallic, ionic or van der Waals [10]. The strongly bonded atoms with the substrate will have low surface mobilities and act as a nucleation site while weakly bond atoms have high surface mobilities and will diffuse, ideally, to preferential nucleation sites where stronger, permanent bonding is possible.

Further growth of the nucleation process is facilitated by either direct impingement of condensing atoms or through migration over the surface to the already formed nuclei. Thus, the material can grow even if deposition is interrupted, despite the drive to achieve the lowest possible thermodynamic state [13]. Typically, grains of the depositing material have different sizes and orientations which will affect the surface and interfacial energies. Atoms from the smaller island atoms will migrate towards the larger island to minimize the interfacial free energy of the system. This process is known as Coarsening or Oswald ripening [10,14].

### **2.3. Growth of coalescent films**

The growth of coalescent films depends upon the strong adhesive force between the substrate and deposited atoms [10]. After the monolayer films are deposited on the substrate, it is followed by another monolayer which is found to be loosely bound to the first layers and so on. Such types of growth are known as Frank-Van der Merwe and typically found in the growth of semiconductor films on semiconductors [10]. Volmer-Weber growth is seen when deposited materials have strong bonding than it does with the substrate. Such growth can be seen when metal is deposited on insulators. Stranski-Krastanov (layer plus island growth) is a cross between the two previously described methods, where after the first few monolayers of newly deposited material abandon this type of growth as being no longer energetically favorable and island growth occurs [13].

The possible cause of the growth of the island is due to change on strain on the deposited films. It can be seen, for example, when nickel is deposited on silicon, silver on tungsten, etc.

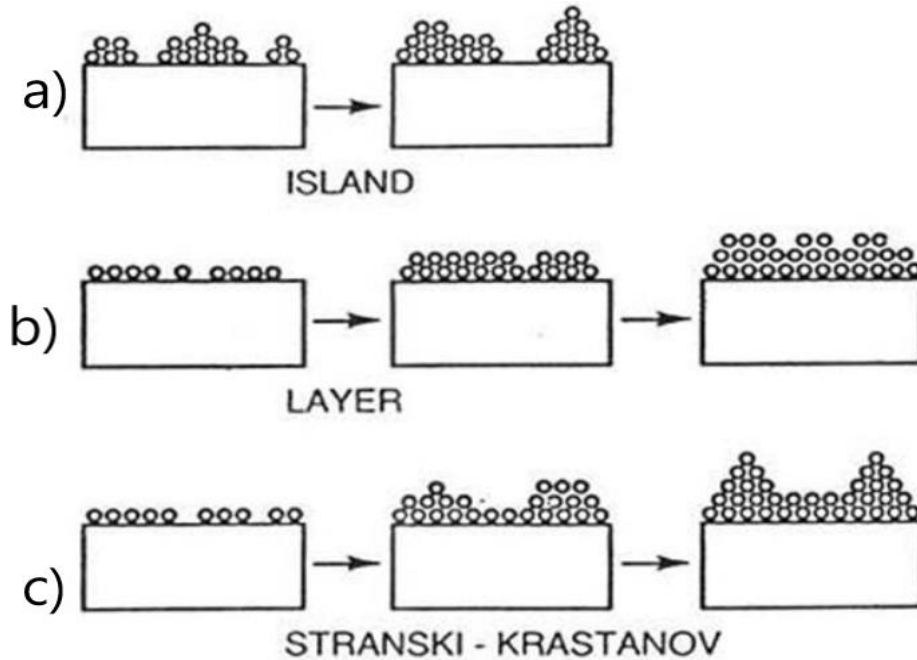


**Figure 3.** Basic Models for thin film growth a) Volmer-Weber Model, b) Frank-Van der Merwe Model, and c) Stranski-Krastanov Model [10].

Thermodynamically, the difference between layer by layer and island growth is the sum of a substrate, interface, and film free energy [10,13]. When the sum of the substrate and interface free energy is greater than the thin film surface energy, then the deposited film spreads over the total energy to maintain the minimum surface energy [15]. Similarly, when the sum of film surface energy and interface energy is greater than the substrate free energy, then the surface tries to minimize the energy by the growth of islands [15,16].

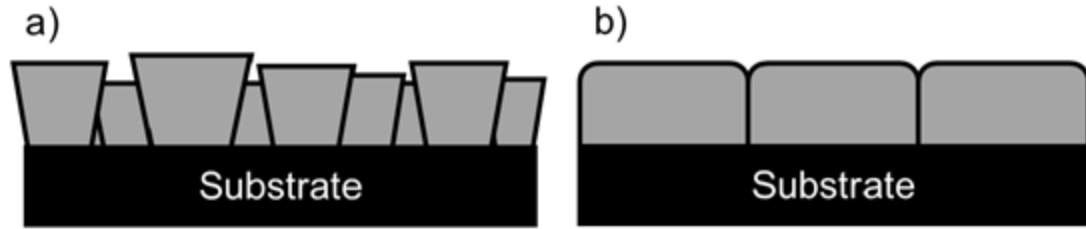


**Figure 4.** Types of thin film growth on a polycrystalline film with a) immobile grain boundaries and b) mobile grain boundaries.

Thin film growth can occur through epitaxial growth of existing grains at low deposition temperatures. Exceptions to this include re-nucleation processes when the surface composition of as grown grains is changing during the deposition. Such instability in the thin film is possible even for films of relatively high purity. Impurities absorbed at the growth surface which are not compatible with the growing material structure will be rejected. Such impurities can act as a nucleation center, accommodated as a defect within the grown crystal, or cause twinning within the growing crystal.

For typically clean growth conditions, the coalescent thin film thickens in two ways depending on if its grains are mobile or not (Figure 4). Materials with firm grain boundaries (e.g., W, Fe, Si) continue the growth of an columnar structure depending on the initial orientation of the nucleated grains. The grain growth is restricted to only the top surface of the grains where differently oriented grains compete, as can be seen in Figure 4. Specifically, oriented grains with preferable fast-growing crystal planes will eventually outgrow the rest and will dominate the surface; this phenomenon was first described and investigated by van der Drift [17].

## 2.4. Thin Film deposition techniques

In this work, for the deposition of nickel film on a silicon substrate and diamond film deposition, two different deposition processes were employed; electron beam evaporation and chemical vapor deposition. Electron beam evaporation (or e-beam evaporation) is a physical vapor deposition process that allows material evaporation that is difficult or impossible to produce using standard resistive thermal evaporation [18]. For example, e-beam evaporation is useful for gold, used in electrical contacts in solar cell applications, or ceramics like silicon dioxide, for optical films, and many more. Electron beam deposition uses a magnet to focus the electron to form a beam, which is then directed towards a crucible that contains the material of interest [18]. The energy of the electron beam is transferred to the materials, which causes it to evaporate. The material's vapor then condenses on and coats the substrate. Figure 5 shows an e-beam evaporator system.



**Figure 5.** Angstrom Engineering Evo Vac [18].

The Chemical vapor deposition technique is used for the deposition of thin film coatings onto a variety of substrates. The most simplified process of chemical vapor deposition consists of a chamber and precursor gases. The chemical reaction occurs near the substrate surface resulting in the formation of thin layers on the substrate. The most promising techniques for large area and good quality diamond films are microwave plasma CVD (MPCVD) and hot filament CVD (HFCVD). In both cases, the carbon carrying gas is methane and dilute hydrogen are precursor gases. The gas inlet and outlet, a rotary pump and resistive filaments are the main components of the HFCVD chamber, as shown in Figure 6. The melting point of the filament should be high, and the substrate should be positioned so that the gas contacts the filaments prior to contacting the substrate surface.

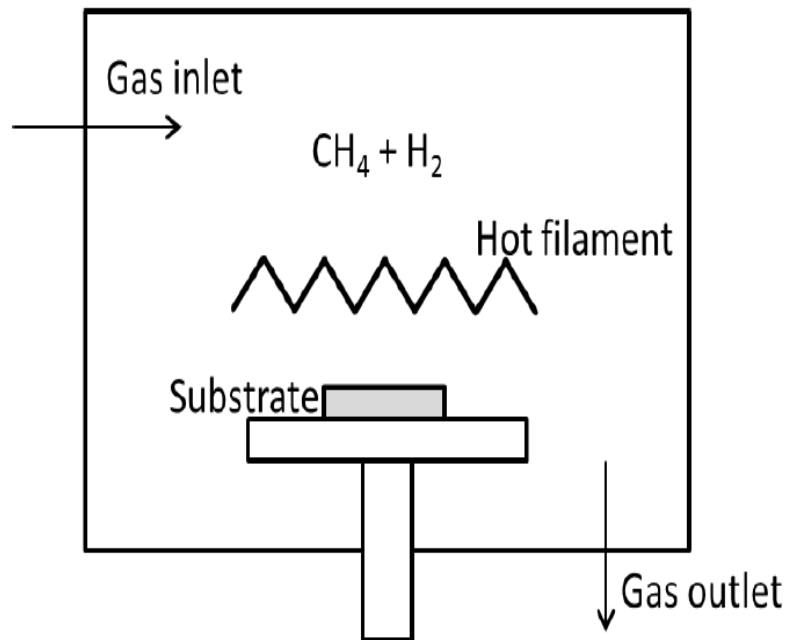


**Figure 6.** Schematic of HFCVD apparatus [10].

The primary role of the filament is to dissociate the  $H_2$  gas molecules at high temperature and also react with the carbon carrying gas to facilitate adsorption on the surface of the substrate [4,10]. The deposition rate of HFCVD is tunable, and HFCVD is easily scalable and can deposit diamond over large areas. The main disadvantage of HFCVD is the presence of filament close to the substrate materials, which may cause contamination during the deposition process [4].



**Figure 7.** Texas State Crystallume CVD system.

The Texas State Crystallume EC-001T CVD diamond deposition system is designed to produce CVD diamond coatings by the HFCVD method with methane as the carbon-containing reactant gas. It has a maximum  $13\text{ cm} \times 13\text{ cm}$  deposition area with typical growth rates of  $0.01\text{-}0.045\text{ }\mu\text{m/h}$  across a  $100\text{ mm}$  wafer [19]. It has a water cooled rotating  $100\text{ mm}$  wafer chuck with the adjustable cooling control and flexible filament to substrate distance [19].

## 2.5. Stress development during thin film deposition

Certain degrees of stress are developed in all amorphous, polycrystalline and single crystalline thin films grown by many PVD techniques. The stress accumulation within the thin film may induce different texture formation within the film. The origin of stress within the film can consist of epitaxial stress (lattice mismatch between the substrate and the film), intrinsic stress (stress developed during the film nucleation and growth) and thermal stress (resulting from different thermal expansion coefficient of the substrate and the thin film) [20].

### 2.5.1. Epitaxial stress

During thin film deposition on a substrate, the epitaxial stress may form when the lattice parameter of the film and the substrate do not match to each other. The stress development during the stress formation at the interface between the thin film and the substrate is given mathematically by the relation [20],

$$\sigma = E_{\text{film}} \cdot \frac{d_{\text{o,sub}} - d_{\text{o,film}}}{d_{\text{o,film}}} \quad [\text{GPa}] \dots\dots\dots (1)$$

Where, ' $d_{\text{o,sub}}$ ' is the lattice constant of substrate, ' $d_{\text{o,film}}$ ' is the lattice constant of the deposited film and ' $E_{\text{film}}$ ' is the elastic constant of the deposited film. When the lattice spacing of the substrate is higher than the thin film, then the stress is tensile; otherwise, it is compressive. The stress development on the polycrystalline film depends upon the nature of the film, deposition conditions, and the level of contamination [21].

### 2.5.2. Intrinsic stress

During the PVD growth techniques, certain types of stress typically develop in all amorphous, polycrystalline, and single crystalline films. The intrinsic stress is not due to lattice mismatch strain, but rather to the growing strain produced between the thin film and the substrate [21]. This stress arises when the film is deposited under a non-equilibrium condition. The typical behavior of the film stress as a function of the film thickness is shown in Figure 8 below.

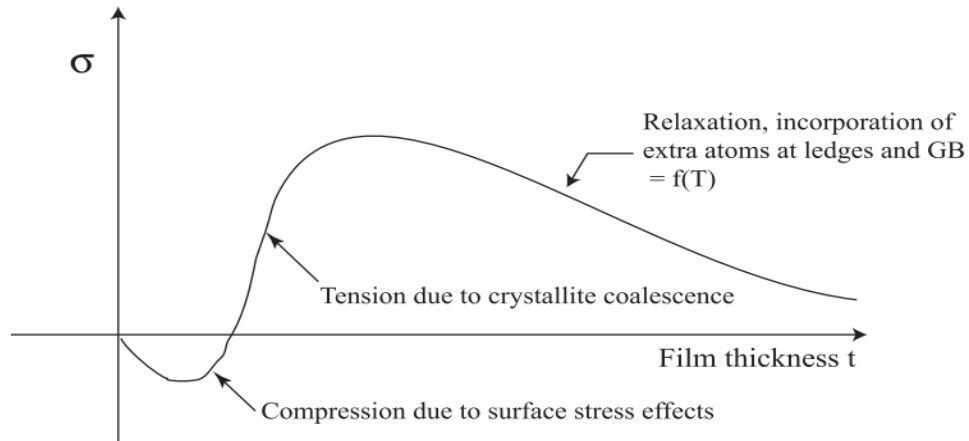


**Figure 8.** The variation of growth stress with an increase in the film thickness [20].

Stress development within the thin film can vary with depth of the deposited film. It is possible to divide stress development into two stages, stress before film coalescence and stress after the film growth.

#### 2.5.2.1 Pre-coalescence stage

The deposited material forms individual islands as separate nucleation sites at energetically favorable locations on the substrate surface during the first stage. This cluster of deposited atoms is under compressive stress due to capillary force being

exerted on the isolated island. The behavior of the deposited islands of solids is analogous to the behavior of liquids on a solid surface and can be described by a modified Laplace formula [11];

$$\Delta p = 2fr \quad [\text{GPa}] \dots\dots\dots (2)$$

where ‘ $\Delta p$ ’ is the Laplace surface pressure, ‘ $f$ ’ is surface stress, and ‘ $r$ ’ is the radius of the cluster/sphere. Surface capillary forces constrain the lattice structure and are the cause of compressive stress. As can be seen from equation 2, with the growing size of the island increasing, the force exerted onto the island decreases [10].

**2.5.2.2. Coalescence stage**

The effect of coalescence phenomena on the thin films deposition process was first identified by Hoffman et al. [20]. They found that when two island surfaces growing at proximity form grain boundaries, the joining process dictates their partial displacement due to the adhesion of the material to the substrate, which imposes elastic strain on the growing crystals. The idea behind the approach is that the net surface free energies for separate grains are greater than the free energy system of joined grains, including relatively low energy of grain boundaries [10,15]. The tensile stress of coalescing grains can be calculated using the size of the gap ( $\Delta$ ) which separates them [20], as

$$\sigma = (E_f/1-\nu) \cdot \Delta/L \quad [\text{GPa}] \dots\dots\dots(3)$$

Where ‘ $\sigma$ ’ is stress, ‘ $(E_f/1-\nu)$ ’ is biaxial film modulus, ‘ $E_f$ ’ and ‘ $\nu$ ’ are Young’s modulus and Poisson’s ratio of the deposited material, respectively, and ‘ $L$ ’ is the diameter of the grain.

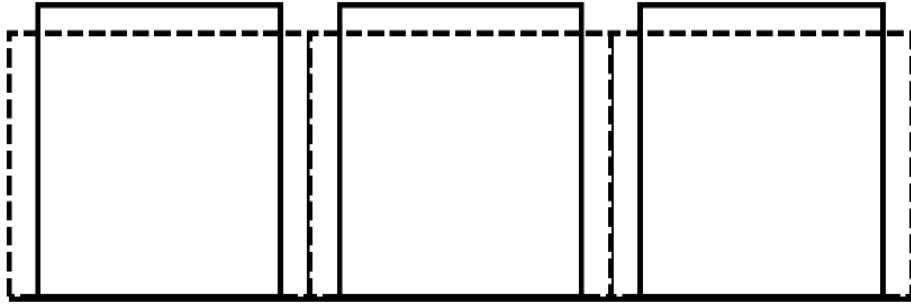


**Figure 9.** Grains of the polycrystalline film before and after coalescence [10].The solid line in the figure represent the grains before coalescence and the dashed lines represent the formation of grain boundaries after grains coalescence.

### 2.5.2.3. Film thickening stage

Stress development in a thin film during coalescence depends upon the atomic mobility of the depositing material (i.e., the adsorbed atom, or adatom) and deposition conditions. For materials with low adatom mobility, the stress value of the coalesced film does not substantially change. As a result, strained thin films are developed. Materials of high adatom mobility, like FCC metals of relatively low melting points, tend not to sustain the tensile stresses imposed from the coalescence stage, which leads to the loss of tolerance, cracking, distortion of thin film [13]. So, the stress development on the films thickening stage depends on the adatom mobilities and tensile stress produced between the coalesced grains boundaries with different deposition conditions [10,13].

### 2.5.3. Surface stress effect

The force per unit length of exposed edge that must be applied in to terminate surface in order to maintain the surface in equilibrium is called surface stress and the reversible work required to create a unit area of surface at a constant temperature, volume, and chemical potential is called surface free energy [20].The relationship between the interfacial energy of a cluster per unit area ( $\gamma_f$ ) to that of the surface ( $\gamma_s$ ) is

given by [17],

$$\gamma_s = \gamma_i + \gamma_f \cos\theta \dots\dots\dots (4)$$

Where ' $\gamma_i$ ' is the unit area energy between the island-like cluster and substrate energy due to the change in interfacial energy, and ' $\theta$ ' is the contact angle between the cluster and substrate.

The surface stress of a thin film can be modified by certain external applications, such as thermal annealing. In general, the solid-state aggregation of the thin film occurs only when there is sufficient driving force; i.e., minimum interfacial energy between the film and substrate. [16,22,23]. For example, the solid-state aggregation of Nickel film cannot proceed under the condition of  $\gamma_s > \gamma_i + \gamma_f \cos\theta$  as a thin Nickel film will aggregate to form island like clusters when the sufficient driving force is achieved[17].

**2.5.4. Stress generation due to coalescence of grains boundaries**

When the film consists of small grains at the early stage of film growth, when these grains coalesce, tensile stress is generated [20]. As grains grow, the gap between them decreases until it is so small cohesion begins to develop between the grains [24]. Sometimes, the cohesion is so strong that the elastic deformation of crystalline grains begins to occur. Thus, the stress between the two contacting spheres of crystallites depends upon the surface free energy and the separation distance between them [20].

**2.5.5. Thermal stress**

When the film on the substrate is subjected to a temperature change, differential thermal expansion will result in thermal stress in film and substrate [10]. It is an extrinsic

type of stress which develops when the coated substrate is brought to a different temperature than the deposition temperature [11]. The nature of stress depends upon the thermal expansion properties of the substrate and deposited film. For an infinitely deep substrate, the thermal stress can be calculated by the relation[11],

$$\sigma_{th} = \frac{E_D}{1 - \nu} \int_{T_1}^{T_2} (\alpha(T)_D - \alpha(T)_S) dT \dots\dots\dots (5)$$

Where ‘ $E_D$ ’ and ‘ $\nu$ ’ are Young’s modulus and Poisson's ratio for the thin film, ‘ $\alpha(T)_D$ ’ and ‘ $\alpha(T)_S$ ’ are thermal expansion coefficients of diamond and substrate, and ‘ $T_2$ ’ and ‘ $T_1$ ’ are deposition and room temperature, respectively.

**2.6. Diffusion of Nickel on Silicon substrate during annealing**

Nickel has seen increasing utilization in IC and Photovoltaic device applications [25]. Nickel can rapidly diffuse on a silicon wafer during thermal processing resulting in the formation of different phases of nickel-silicide due to the high solubility and diffusivity of nickel on silicon. [26]. Epitaxial NiSi<sub>2</sub> is the first phase that forms at 200 °C. With increasing temperature, the coexistence of NiSi and NiSi<sub>2</sub> phases is observed in the range of 200-650 °C [26,27]. Above 600°C, the NiSi layer is entirely consumed to form NiSi<sub>2</sub>. The stable form of NiSi<sub>2</sub> can be observed after heating in the temperature range of 700-800 °C for several minutes. (111) or (100) Si wafer followed by annealing at different temperatures.

The silicidation process of Ni on Si substrate has been well established in the literature [25–27] and is shown in Figure 10. It is worthwhile noting that the published results are produced by depositing rather thick (>30 nm) Ni film on(111) or (100) Si

wafer followed by annealing at different temperatures. The reaction of Ni with Si typically proceeds through the following steps [26]:

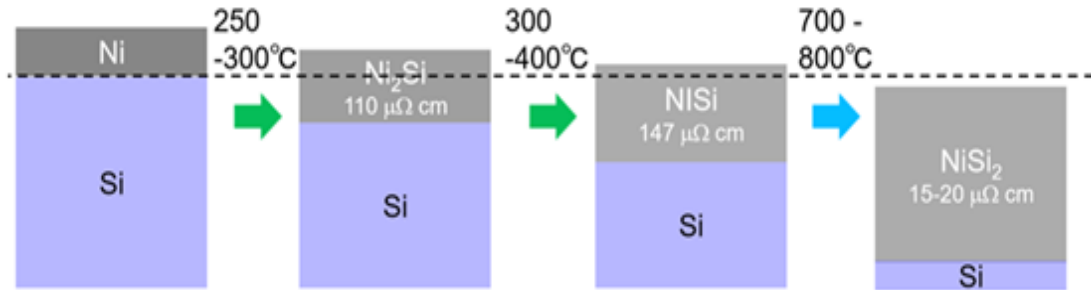
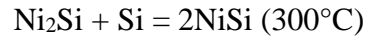


**Figure 10.** Nickel Silicide phase changes with different annealing temperature [28].

Nickel mono-silicide (NiSi) tends to grow faster on (100) than (111) silicon [26]. It has the lowest electrical resistivity compared to the other nickel-silicide phases and is implemented extensively in device fabrication. NiSi is stable up to 750 °C, above which the nucleation of NiSi<sub>2</sub> begins. NiSi<sub>2</sub> can be grown epitaxially on both (100) and (111) oriented silicon substrates [25]. The phase diagram described by Massalski [28], and shown in Figure 11, is composed of 13 phases and, critical to the present research, exhibits a eutectic point at 966 °C. [31]

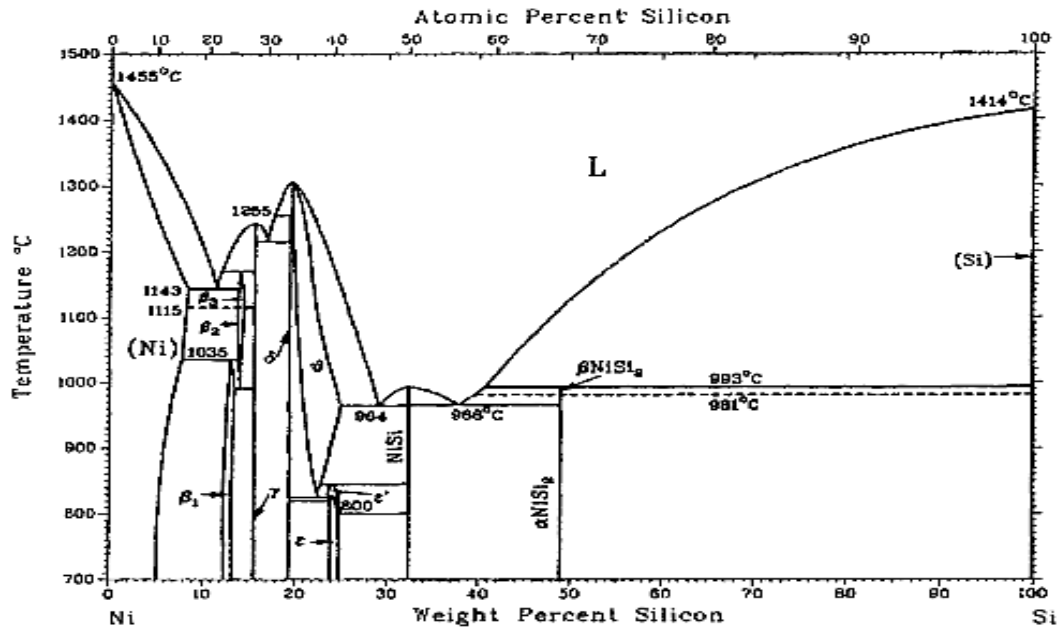


Figure 11. Ni-Si equilibrium phase diagram [29].

## 2.7. Texture development in thin films

Thermal annealing is an essential source of stress in thin films. Thermal stress is mainly induced by the mismatch between the thermal expansion coefficients of the thin film and substrate [30]. The correlation between the development of stress variation and texture formation on the thin film surface by annealing is a result of grain growth. The microstructure transition during annealing has been reported by many researchers [30,31]. For FCC metals, the texture is developed along with the grain structure with strong (111) crystallographic orientation [30]. It has been found that grains with low surface and interfacial energies dominates the film texture. This orientation dependent driving force is of great importance because it strongly affects the texture of a film as well as the rate of grain growth [32]. For FCC metal films, the orientation with the lowest surface energy is along (111), and thus the strong (111) texture typically

obtained in FCC metal thin films is attributed to the minimization of energies at the free surface and film–substrate interface [30].

## **2.8. Nucleation and growth of diamond film**

Diamond nucleation and growth are two different processes which can be performed with different parameter settings. The change in the quality of diamond film with the variation of parameters during nucleation and growth has been explained by various research groups [33–35]. The critical factors that need to be considered during the deposition of diamond on the non-diamond substrates are the state of the sample (surface roughness, cleaning process) and CVD deposition parameters (gas pressure, reactant gas, total gas flow and position of the sample in the chamber) [10,34].

### **2.8.1. Diamond nucleation**

Typically, a high concentration of diamond nuclei on the substrate is desired prior to diamond deposition to achieve a denser diamond film with high growth rate with better mechanical and optical properties, fewer defects and smoother surface. The nucleation stage differs from the diamond growth stage and depends upon the nature of the substrate and/or diamond seeding [10]. Diamond has a high surface energy and low sticking probability, so it is not readily nucleated on smooth surfaces such as silicon [10].

Many pre-treatments have been invented to overcome the low sticking probability and to overcome the diffusion of carbon atoms into the substrate materials and to enhance the density of diamond nuclei created in the initial stage of diamond growth. These methods include scratching (using diamond or other abrasives), ultrasonic agitation (using diamond nanoparticles and/or other abrasives), surface biasing, chemical etching

of the substrate surface, deposition of interlayers (thin metal films, boron nitride, carbides, and different carbon species) and many others [36,37]. The nucleation of diamond typically includes the following steps:

### **Step I – Formation of carbon clusters**

Carbon clusters are formed on the substrate surface due to the constant atomic hydrogen bombardment, causing a change in local thermal conditions. Thereby, there is a change in carbon structure from  $sp^1$  to  $sp^2$ .

### **Step II – Conversion of $sp^1$ to $sp^2$ and then to $sp^3$ bonding**

Molecular bombardment of activated hydrocarbon and atomic hydrogen gives the substrate sufficient energy to transform  $sp^2$  bonded carbon into  $sp^3$ . Atomic hydrogen promotes this reaction and stabilizes the  $sp^3$  phase. Etching of all three carbon phases ( $sp^1$ ,  $sp^2$ , and  $sp^3$ ) is taking place at the same time. However, the etch rate of the less stable  $sp^1$  and  $sp^2$  phases is ten times faster than etching the  $sp^3$  phase [10].

### **Step III – Crystallization of amorphous phase**

For crystallization to happen, the carbon bonding undergoes a transition stage from  $sp^2$  bonded carbon, to disordered domains with  $sp^3$  bonded carbon and finally to  $sp^3$  bonded carbon. Carbon atoms must rearrange themselves during the recrystallization process to acquire minimum surface energy. This rearrangement should favor (111) crystallographic orientations since (111) orientation has the lowest surface-free energy in the diamond crystal. The recrystallized region becomes a nucleus for subsequent diamond growth.

For the non-diamond seeded substrate, the nucleation stage can be divided into several sub-stages: a) Incubation period, b) 3D surface nucleation, c) termination of

nucleation and 3D growth of nuclei to grains, and d) faceting and coalescence of individual grains and formation of continuous films [10]. The diamond nucleation can happen on the non-diamond substrate if the substrate surface is saturated with carbon and high energy sites such as active vacancies, dangling bond, and active sites are present.

### 2.8.2. Diamond growth

The important aspects of the diamond growth stage are the diamond growth rate and diamond quality [10]. Production of better-quality diamond films that takes shorter times is the interest of current research. For high purity diamond films, 0.5-1.5 volume percentage of methane to hydrogen is recommended [38]. However, the low methane concentration slows the diamond deposition process considerably because the effect of atomic hydrogen is dominant. Other notable diamond deposition conditions include pressure in the range of 10-150 Torr with a substrate temperature of 700-1100 °C [1,10].

**Table 1.** Parameter range for diamond synthesis by filament HFCVD method [1].

Gas Mixture	Total pressure (Torr)	Substrate Temp.(°C)	Filament temp.(°C)
H <sub>2</sub> +CH <sub>4</sub>	10-100	700-1000	2000-2300

The general scheme for the deposition of diamond [1] by CVD is shown in Figure 12, where the hydrogen and methane undergo activation leading to dissociation. The activated gas species are transported through diffusion, forced flow, and/or convection to the substrate surface whereby multiple reactions, such as adsorption, desorption, and diffusion will take place.

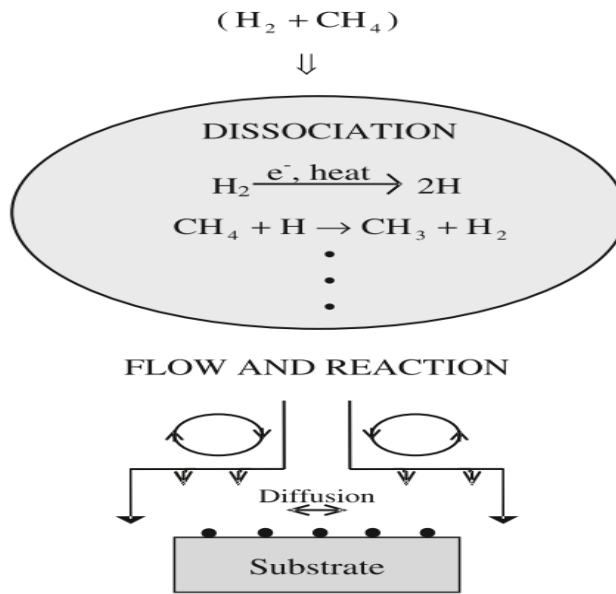
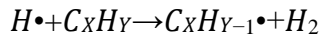


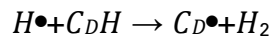
**Figure 12.** Schematic of the process occurring in CVD diamond [1].

The generic model [39] which describes the formation of diamond is well known through the following set of equations:

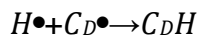
- i. Formation of free radicals,



- ii. Hydrogen adsorption from activation site (C<sub>D</sub>)



- iii. Addition of hydrogen to the diamond surface



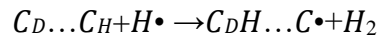
- iv. Addition of hydrocarbon radicals to the diamond



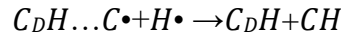
The surface bonds are initially hydrogen terminated, followed by hydrogen absorption with the addition of hydrogen or hydrocarbon radicals on the diamond surface. (The replacement of hydrogen in the diamond surface is more than the addition of hydrocarbon

radicals on the activated diamond sites [10]. The sequence of reactions (i)-(iv) leads to the addition of radical hydrocarbons to the surface [40]. The process of chemisorption of newly added hydrocarbon species to the adjacent terminated diamond site ( $C_DH...CH$ ) happens through the process of hydrogen removal and rearrangement of added hydrocarbon atoms.

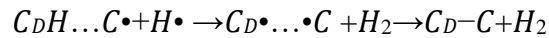
- v. Hydrogen adsorption from the adjacent diamond site,



- vi. Hydrogen addition to the adjacent diamond site,



- vii. Hydrogen adsorption from the diamond site and formation of new carbon to carbon bond,



The most commonly used process gasses include hydrogen/methane, argon/methane, or hydrogen/argon/methane [1]. The reaction rates depend upon the concentration of atomic hydrogen species. Hydrocarbon species supplies the necessary carbon atoms for the diamond formation during the diamond synthesis from the gas phase. Argon is often used as the main atmosphere volume with a small hydrocarbon gas concentration, or combination with a small amount of hydrogen. The effect of an argon rich atmosphere is like the effect of increasing hydrocarbon gases within the system or lowering the plasma density. They all lead to lowering the size of diamond grains within the nanoscale regions [1].

Oxygen addition in the form of  $\text{CO}_2$ ,  $\text{CO}$ , or  $\text{O}_2$  improves the diamond growth rate and quality. The deposition temperature is typically lower for oxygen additive CVD growth processes, but too much oxygen in the chamber may cause oxygenation of the diamond substrate and diamond coating destruction. Halogen addition in the form of halogenated precursor gases has a similar effect to the oxygen. It was found that their addition allows the use of lower CVD deposition temperatures (250-600) °C. The halogen precursor also increases the diamond growth rate and purity. Similarly, nitrogen incorporation in the diamond lattice increases the intrinsic stress within diamond film through the formation of vacancy defects through the distortion of the diamond lattice [1]. The diamond growth rate is slower than in case of pure  $\text{H}_2$  and  $\text{CH}_4$  atmosphere, which is due to the formation of HCN from  $\text{CH}_3$  radicals, which are more energetically preferable and, therefore, acting as a carbon sink and slowing the diamond deposition rates [35].

## 2.9. Texture Development in CVD Diamond

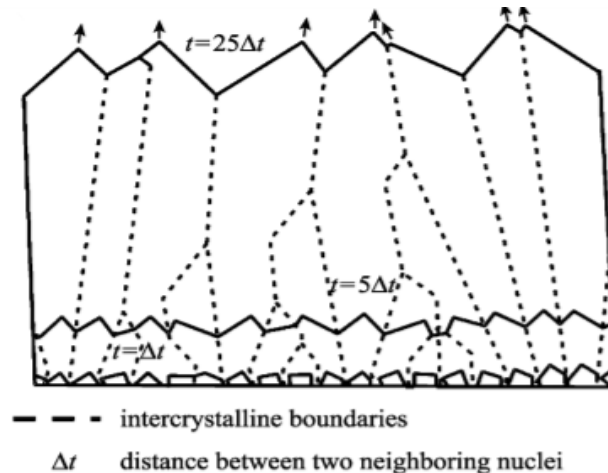


**Figure 13.** Schematic model for the development of thin film by Van der Drift [41].

The crystallographic direction with the highest growth rate in the normal substrate direction will favor strong texturing of the sample normal direction [42]. The texture development of the diamond film can easily be understood through the Van Der Drift evolutionary model [41–43]. It explains about the grains that grow fastest vertically overtake smaller grains and overtake the orientation of the film [43]. The growth process is kinetically driven and depends upon the surface energy, multiplicity of growth planes, and deposition parameters [42].

**Table 2.** Possible transformation by primary and secondary twinning [43].

Twinning	Rotation angle/axis	Change of lattice plane after primary and secondary twinning
Primary ( $\Sigma 3$ )	$60^\circ/(111)$	$\{001\} - \{221\}$ (1st) — $\{148\}, \{447\},$ or $\{001\}$ (2nd) $\{110\} - \{110\}$ or $\{114\}$ (1st) — $\{110\}, \{114\}, \{778\},$ or $\{4,5,11\}$ (2nd) $\{111\} - \{111\}$ or $\{115\}$ (1st) — $\{111\}, \{115\}, \{11,11,1\},$ or $\{5,7,13\}$ (2nd)
Secondary ( $\Sigma 9$ )	$38.9^\circ/(110)$	$\{001\} - \{447\}$ or $\{148\}$ $\{110\} - \{110\}, \{114\}, \{778\},$ or $\{4,5,11\}$ $\{111\} - \{115\}, \{5,7,13\},$ or $\{11,11,1\}$

The growth mechanism in (111) and (100) planes was studied by Liu et. al. (2009) [43] using the DC arc jet technique. They found that deposition along (111) planes occurs via the interactions of radicals with at least one free bond ( $\text{CH}_3, \text{CH}_2, \text{CH}, \text{C}$ ) and one radical with at least three  $\text{CH}_1$  or C. Similarly, growth along the (100) direction proceeds with two  $\text{CH}_2$  bonds. It has been found that the formation of twins and micro twins during the growth process also affects the texture of the films suggested by the Meakin Growth model [44] for the texture development along (110) orientation. The most common twinning planes can occur along (111) and (110) orientation, as indicated in Table 2.

A variety of textures, including (111), (100) and (001), have been reported for diamond growth by HFCVD, although the exact parameters are generally guarded [42,45]. They reported that  $\langle 111 \rangle$  and “cauliflower”  $\langle 110 \rangle$  textured films suffer from a high density of twinning, where  $\langle 100 \rangle$  films are much more stable to defects. The texture developed along the (001) direction with increasing substrate temperature is reported for the hot filament and DC arc methods. Similarly, elevated methane concentration and film thickness associated with (110) texture have been reported by Liu et al. [43].

### **3.0. Heteroepitaxial growth of diamond films on a nickel substrate**

The heteroepitaxial growth of diamond films on non-diamond substrates has been sought due to potential applications in microelectronic devices. Some of the possible candidates for the heteroepitaxial growth of diamond films include Mo, Ni, Cu, cBN, BeO, etc. [5]. The most extensive experiments have been done on these substrates, but the results have been randomly oriented diamond films. The high energy between the diamond and non-diamond substrate for the principle lattice planes and the existence of interfacial misfit are the possible causes for the randomly oriented diamond films [5].

The lattice constant of nickel ( $3.517 \text{ \AA}$ ), differs by only 1.2 % with that of diamond ( $3.567 \text{ \AA}$ ) and acts as a catalytic metal solvent for high-pressure and high-temperature (HP-HT) diamond synthesis [4,5]. Hence, nickel is promising for heteroepitaxial growth of diamond films. However, graphitic interlayers tend to form on the Ni substrate when placed in the methane-hydrogen CVD environment. The nucleation of diamond films on graphitic interlayers forms a partial orientational relationship between the diamond and non-diamond substrate. It has been known for decades that Ni

is an effective solvent-catalyst metal for diamond crystallization under HP-HT conditions. Although a detailed mechanism of the solvent-catalytic effect has not been completely developed, it is believed that it is based on the strong reactivity with carbon. Thus, it is interesting to consider if this same characteristic can be utilized in a low-pressure CVD process.

Indeed, Badzian et. al. [46] have recently performed a study of diamond deposition on thin films of Ni and found that when Ni forms nickel hydride, the graphite formation can be inhibited in a CVD environment. Sato et. al. and Fujita et. al. [4] also reported that both (111) and (100) oriented diamond nuclei could be grown on Ni substrates, but the amount of orientation was somewhat limited, and no details were given about the deposition process. In addition, several recent theoretical papers on reactions between Ni and hydrogen or hydrocarbons have provided further momentum for this research subject.

### **3.1. Characterization techniques**

There are various techniques available for the characterization of diamond films. The applied techniques for the characterization of diamond films include ellipsometer, scanning electron microscopy, Raman spectroscopy, x-ray diffraction techniques, surface profilometer, and atomic force microscopy are described in this section.

#### **3.1.1. Scanning Electron Microscope**

Scanning Electron Microscope (SEM) is an essential tool for the study of the surface and the near surface regions of thin films. The electron gun emits a beam of electrons which are accelerated by the presence of an anode. The electron beam is

focused by a set of electromagnetic lenses which are implemented by a magnetic coil. The used accelerating voltage by the electron beam is typically in the range of 1-30KeV [10] and among other things determine the beam size and resolution of the microscope.

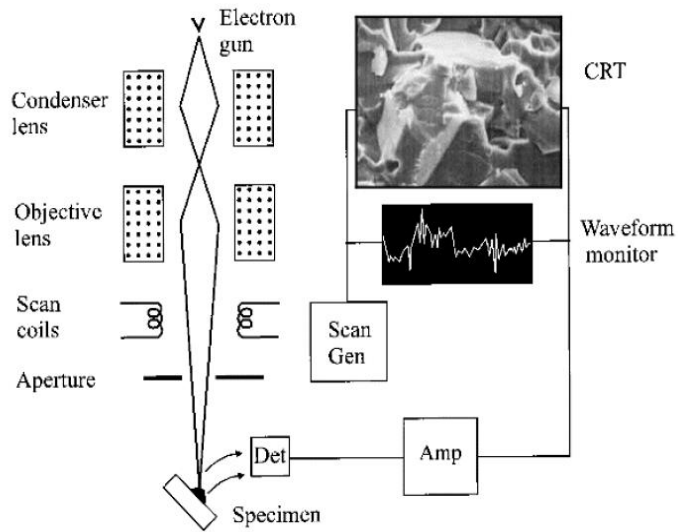


**Figure 14.** The schematic diagram for the main parts of the scanning electron microscope [47].

The scan coils divert the beams to form a scanning pattern on the surface. The electrons are impacting the surface and the near surface region of the sample and react with the atoms within the sample under study [47]. A variety of interactions can be used as a signature providing information about the sample. The interactions of the electrons beam with the samples atom produce many secondary electrons such as Auger electrons, cathodoluminescence, secondary electrons, backscattering electrons, and x-rays [10,47]. SEM can also be used for the chemical analysis of the sample. There are two types of instruments being used for the chemical analysis using X-rays, Energy-Dispersive Spectroscopy (EDS) and Wavelength Dispersive Spectroscopy (WDS).

Both EDS and WDS measure the x-rays emitted from the sample. EDS uses an energy height detector that can determine the number of photons per second in a certain energy range. WDS uses some form of diffraction device to separate out photons with different wavelength. The resolution of WDS is significantly better than that of EDS. The depth of focus of the SEM is far better than the resolution of an optical microscope [47]. For high laterals and spatial resolution images, scanning electron microscope with a minimum electron wavelength is used. EDS can measure all arriving energy X-rays from the sample at the same time, but the WDS can measures the counts for the arriving X-rays for specific wavelengths. The depth of focus of the scanning electron microscope is far better than another optical microscope [47].For high laterals and spatial resolution images, scanning electron microscope with minimum electron wavelength is used.



**Figure 15.** FEI Helios Nano lab 400 Scanning electron microscope at Texas State.

For this research, a Helios Nano lab 400 SEM furnished with an EDAX was used. This microscope has capabilities to take scans for both conductive and nonconductive samples. It is a fully digital Field Emission SEM (FEI SEM) equipped with Focused Ion Beam (FIB) technology. The dual beam platform is used for sample preparation, imaging, and analysis in semiconductor failure analysis, process development, and process control. It has an ultra-high resolution which is capable of 0.9 nm at an optimal working distance (15 kV) of 1.0 nm at the dual beam coincident point and 350 V – 30 kV beam voltage range.

### 3.1.2. Atomic force microscopy

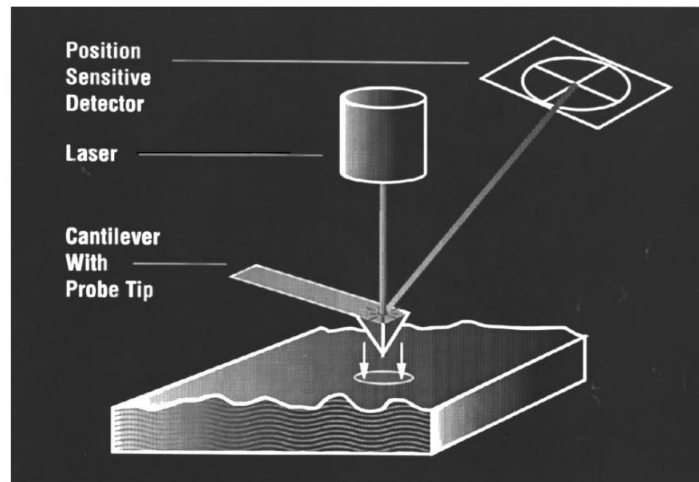


**Figure 16.** General block diagram of AFM working principle [50].

Atomic force microscopy (AFM) belongs to the group of scanning probe microscopy techniques in which the resolution can be down to the atomic scale if careful sample preparation and measurement conditions are fulfilled [10]. The working principle for AFM is based upon the repulsive forces formed between two objects when they are brought closer. An AFM consists of a scanning probe which consists of a cantilever with

a sharp tip, typically made up of different metals. The tip is in continuous or intermittent contact with the sample during the scan depending on the choice of the scanning mode.

A laser beam is focused on the back of the cantilever tip and deflected from the cantilever tip and deflected from it toward a four-quadrant optical detector [48]. For optimum detection surface morphology, the laser beam should be aligned appropriately. AFM has three primary modes, force measurement, imaging, and manipulations [48]. The force between the tip and the sample as a function of separation distance is considered for the force measurements. The force between tip and sample can be used to control the property of the sample in a controlled way and be used of atomic manipulation of the sample [50].



**Figure 17.** Bruker atomic force microscope at Texas State.

For this research, a Bruker AFM was used, shown in Figure 17, which has sub nanoscale characterization and imaging capabilities on a large sample scanning platform. The temperature compensating sensors on the system helps to reduce the measurement

noise and drift allowing it to produce quality images and helps to characterize exact surface morphologies of samples under study. It has the capability scans of  $92\ \mu\text{m} \times 92\ \mu\text{m}$  with  $1\ \mu\text{m}$  scan range.

### 3.1.3. X-ray diffraction

All existing materials have different properties like structural, physical, mechanical, thermal, and electrical, etc. These properties must be studied to understand better how different materials can meaningfully be applied in devices. Different analytical tools have been invented to study the structural, physical, morphological, optical, and electrical properties, etc. Of these, the study of structural properties becomes important as they determine the remaining properties of the materials. X-ray diffraction is a tool to study the order of atoms in materials and learn more of the materials crystal.

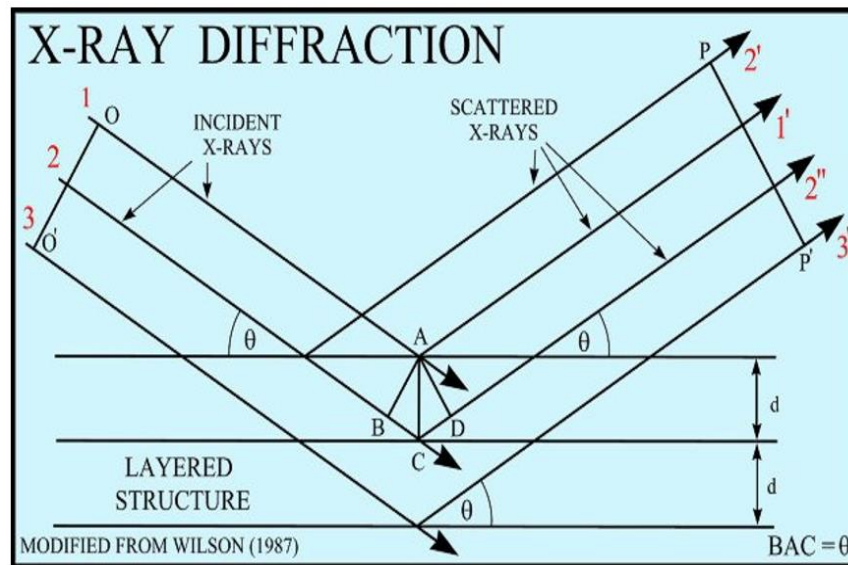


Figure 18. X-rays diffraction [49].

The technique uses a monochromatic beam of X-rays which is directed on the sample surface at the specific angle. The X-ray interacts with the sample as a light beam interacts with a grating and, diffraction effect reveals the information of the crystal structure of materials under study. In the case of the suitable orientation of crystallographic planes within the sample, the X-rays are reflected constructively and are detected by the XRD equipment. As an X-ray beam travels through any substance, its intensity decreases with the distance traveled through the substance. Only a small range of characteristic X-rays are widely used for diffraction. X-rays are created with an x-ray tube, in which an electron beam is accelerated towards a target by a high electric potential. Upon impact, the electrons will excite and ionize some of the target atoms creating element-specific x-rays of a specific wavelength. When the voltage on an X-ray tube is increased above a specific value, then the wavelengths of characteristic lines of target metal are obtained.

These characteristic lines are denoted by  $K_{\alpha}$ ,  $K_{\beta}$ , and  $K_{\gamma}$ . These characteristic lines were discovered by W.H. Bragg. He and his son W.L. Bragg have done foremost experimentation of finding out the crystal structures of NaCl, KCl and KBr, etc. [10,49]. The famous Bragg's law was formulated based on which the diffraction studies are carried out. The condition of constructively diffracting X-rays must fulfill Bragg's Law [49]:

$$2d_{hkl}\sin\theta=n\lambda \dots\dots\dots (6)$$

Where, '  $\lambda$  ' is the wavelength of incident radiation, '  $\theta$  ' is the angle of incidence, '  $d_{hkl}$  ' is interplanar spacing between two adjacent crystallographic planes and '  $n$  ' is an integer.

The integers should be on whole numbers in order to X-rays to be diffracted constructively.

In this research, a Rigaku Smart lab X-ray diffractometer was used to characterize the crystal structure and orientation of the diamond film. The software used on this tool has capabilities to users through both data acquisition and analysis. This tool has some specific hardware features along with an x-y stage for mapping samples, a small angle X-ray scattering vacuum path, a domed hot stage capable of reaching 1100 degrees Celsius, and a 2D detector. The maximum size sample that can be analyzed is a 159mm diameter wafer having a thickness of 3.5mm.



**Figure 19.** Rigaku Smart Lab X-ray diffraction tool in Texas State.

#### **3.1.4. Raman spectroscopy**

Raman spectroscopy is a powerful technique for molecular identifications and structural properties evaluations. The principle for this tool is based upon the molecular interaction with the electromagnetic field of incident radiation and vibrates at

characteristic frequencies of those materials. Lasers of single radiation frequencies are used to irradiate the sample resulting in excitation of molecules in different excitation state or vibrational states. In 1928, Chandrasekhara Venkata Raman discovered the phenomena of Raman spectroscopy. It is a simple phenomenon in which monochromatic light is focused on the sample surface, and the inelastically scattered light is analyzed. Raman spectra are observed in the UV-visible region and are concerned with the vibrational transitions that appear in the  $10^4$  to  $10^2$   $\text{cm}^{-1}$  regions [50]. The spectrum consists of Rayleigh scattering that has the same frequency as the incident radiation and a weak line corresponding to the Raman scattering that has a shift in frequency. Depending on the increase or decrease of the frequency, the lines are called Stokes or anti-Stokes, respectively. Usually, Raman spectra are observed for the vibrational and rotational transition [10,49]. A transition is said to be infrared active if there is a change in the dipole moment of the molecule and is Raman active if there is a change in polarizability of the molecule.

**Table 3.** Raman peaks for diamond and non-diamond carbon[53].

<b>Peak position (<math>\text{cm}^{-1}</math>)</b>	<b>Typical FWHM (<math>\text{cm}^{-1}</math>)</b>	<b>Peak Identification</b>
1100-1150	40-80	trans-polyacetylene
1332	5-10	Diamond ( $\text{sp}^3$ )
1345	250	D peak ( $\text{sp}^2$ )
1430-1470	80	Trans polyacetylene
1520-1580	100	G peak ( $\text{sp}^2$ )

Raman spectroscopy is a handy technique in the field of carbon materials [51]. The most dominant peaks in Raman spectra for diamond and amorphous carbon materials are shown in Table 3. G and D peaks are signals generated by  $\text{sp}^2$  bonded carbon atoms, and their respective abbreviations stand for graphitic (G) and disordered (D) carbon. The

G peak originates from stretching vibration of  $sp^2$  sites which can be in the form of aromatic rings or C=C bonds. The D peak originates from breathing mode of only the  $sp^2$  sites in the form of rings [50,51]. An essential fact about the interpretation of Raman spectra, where diamond and  $sp^2$  carbon sites are present, is the intensity difference between the  $sp^2$  and diamond bonded carbon, which depends on the laser wavelength. In case of visible and near-infrared light, the  $sp^2$  sites can easily dominate and even overshadow the diamond peak due to the higher polarizability of  $\pi$  states over the  $\sigma$  states, which results in  $sp^2$  sites having 50-250 times larger intensities than  $sp^3$  diamond sites [52,53]. On the other hand, ultraviolet light source, the light's wavelengths are low enough to excite the  $\sigma$  states of both  $sp^2$  and  $sp^3$  sites, which gives a more informative view about the  $sp^3$  bonded carbon in the films [52].

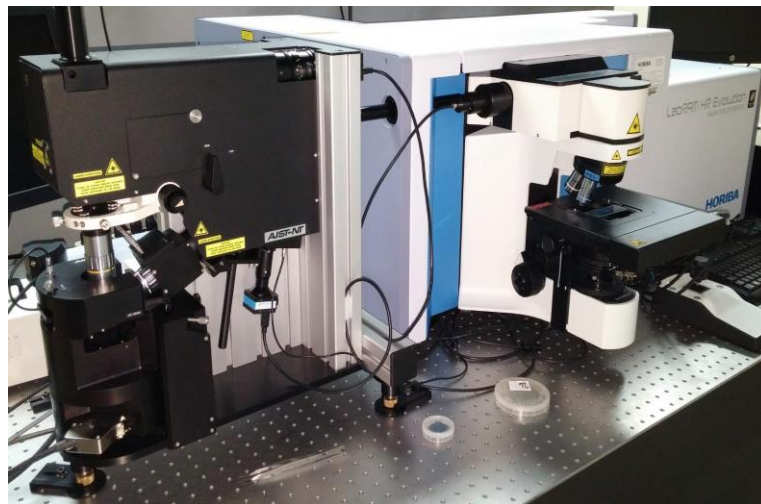


**Figure 20.** Horiba Lab RAM HR Raman spectroscope at Texas State.

The Raman spectroscopy instrument used for this study is a Horiba lab RAM HR Raman spectroscopy, shown in Figure 20. It has capabilities for imaging in both 2D and 3D. It has three excitation lasers with wavelengths of 532 nm, 633 nm, and 785 nm with high

spectral resolution less than  $0.5 \text{ cm}^{-1}$ . It has a scan range up to  $100 \mu\text{m}$ , and the largest sample size of  $25 \text{ mm}$  can be used.

### 3.1.5. Ellipsometry

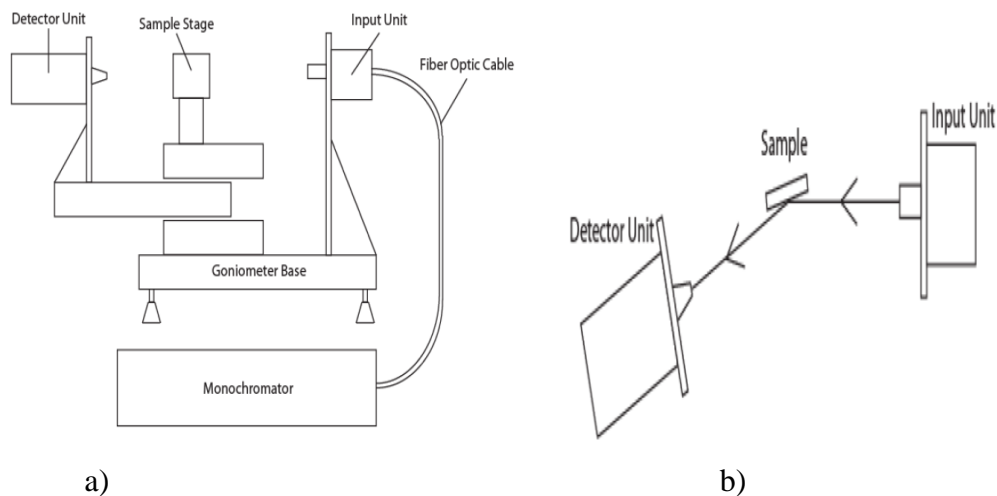


**Figure 21.** The schematic diagram for Ellipsometer set up a) Variable angle spectroscopic tools and b) overhead view of variable angle spectroscopy [54].

Ellipsometry involves the analysis of the change in the state of polarized light that accompanies reflections from the sample surface. The state of polarization can be defined by the phase and amplitude relationships between the two orthogonal component plane waves in which the electric field oscillations are resolved [54]. The theory of Ellipsometry is based on Fresnel reflection and transmission equations of polarized light on the planar interfaces of a multilayer material [54].

The term Ellipsometry comes from the fact that the reflected light of incident linearly polarized light arriving on a surface at an oblique angle is often elliptically polarized. The change of the state of polarization of the light upon reflection depends on the optical properties and structure of the multilayer. Incident light impinging on the

sample is linearly polarized with equal amplitudes of both S and P polarizations [54] [55]. The incident waves are denoted by ‘P,’ for the wave in the plane of incidence and ‘S,’ for the wave normal to the plane of incidence. In general, reflection causes a change in relative phases between P and S waves and change in the ratio of their amplitude. The state of polarization of the reflected light is denoted by the two parameters, the angle  $\Delta$ , which defines the phase shift difference between ‘P’ and ‘S’ polarized light, and the angle  $\Psi$ , the arctangent of the amplitude ratio changes of ‘P’ and ‘S’ polarized light after reflection. The relation between  $\Delta$  and  $\Psi$  is given by [54],

$$\tan(\Psi)\exp(i\Delta) = \frac{(N_1 \cos\theta_2 - N_2 \cos\theta_1)}{(N_1 \cos\theta_2 + N_2 \cos\theta_1)} / \frac{(N_1 \cos\theta_1 - N_2 \cos\theta_2)}{(N_1 \cos\theta_1 + N_2 \cos\theta_2)} \dots\dots\dots (7)$$

Where, ‘ $N_1$ ’ and ‘ $N_2$ ’ are the complex refractive index of air and the sample respectively, ‘ $\theta_1$ ’ and ‘ $\theta_2$ ’ are the angles of incidence at the air to film surface and at the film to substrate interface. The equation is used to determine the complex refractive index of the film.



**Figure 22.** J.A. Woollam ellipsometer at Texas State.

The ellipsometry used for this project is J.A. Woollam ellipsometer pictured in Figure 22. It has a wavelength range of 245-1690nm with CCD detector. The incidence angle can be varied from 20 to 90°.

### 3.1.6. Surface profilometry

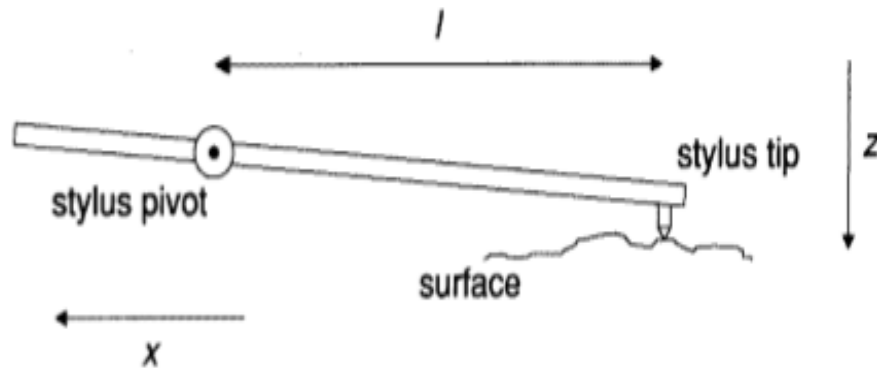


**Figure 23.** A schematic diagram of the stylus profilometer measurement set up along length  $L$ , with scan axis  $x$ , and displacement axis [56].

A profilometer is a highly specific metrological measurement device that is used for the determination of the thickness and roughness of a thin film. It is a very precise instrument as it is expected to have the ability to find or quantify the small-scale surface features. The primary uses of the surface profilometer are focused on characterizing surface's profile to quantify its roughness. Critical dimensions as step size, curvature, flatness are computed from the measured surface profile [57]. A typical profilometer requires the probe tip to be in direct contact with the sample surface, thus making it potentially a destructive measurement technique [57]. A systematic diagram of a simple stylus profilometer measurement set up is shown in figure 23.

For this research, the profilometer used was a Dektak XT surface profilometer. The instrument was used to determine the surface roughness and the thickness of the diamond films at a different position on the samples. The Dektak XT profilometer is an advanced thin and thick film step height measurement tool which can measure the roughness on the nanometer scale. It can provide the step-height with repeatability of  $5\text{\AA}$ . It is equipped with an automatic X-Y stage and theta stage which allows 2D to 3D scans as well. The principle of the profilometer is based upon the surface contact measurement technique where a deflection force (1-15mg) stylus is dragged across the sample surface.

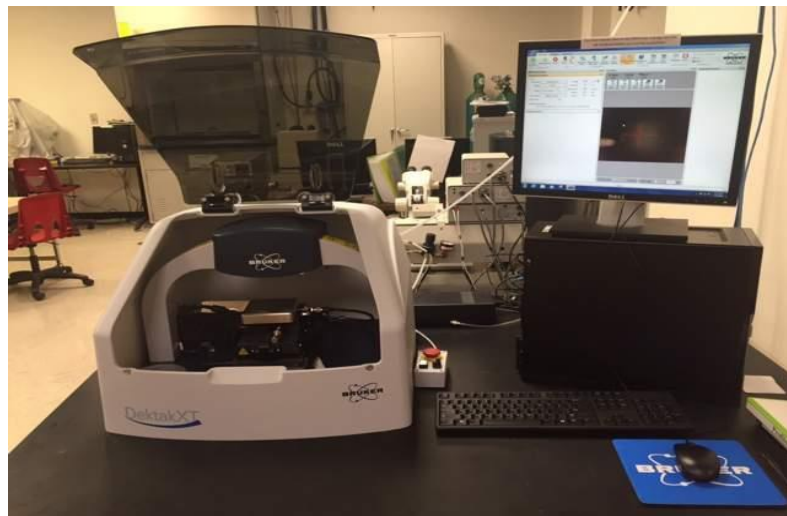


**Figure 24.** Dektak XT Surface profilometer at Texas State.

### III. EXPERIMENTS

The first set of experiments focused on the growth of diamond films on annealed seeded wafers with a thin intermediate nickel modification layer. Textured and self-aligned arrays of Ni nanodots on a silicon wafer were produced by conventional annealing of thin Ni films in the presence of a nitrogen atmosphere. The sample was prepared by depositing thin Ni films of various thickness (5 nm, 10 nm, 15 nm, 20 nm) on (111) oriented P-type silicon wafers. The chamber pressure and Cryo temperature of the instrument during deposition were  $3.63 \times 10^{-8}$  Torr and 10 K, respectively. The rate of deposition was 0.5 Å/s. After deposition, thickness, surface roughness and morphology of the deposited films were characterized by ellipsometry, XRD, and AFM.

After initial Ni film characterization, the samples were annealed in a Lindberg Blue three zone tube furnace at 800 °C for 30 minutes in the presence of 20 psi nitrogen gas. The purpose of annealing was to ascertain the texture and phases developed by the thin Ni film before diamond growth. The annealed samples were characterized by SEM, AFM, and XRD. The phases of the annealed samples were characterized by x-ray diffractometry by taking scans on both medium resolution wide angle parallel beam mode and general  $\theta$ -2 $\theta$  Bragg-Brentano scans at different wafer positions using the X-Y stage. The diamond thin film was grown using the hot filament CVD (HFCVD) method using methane, hydrogen, oxygen, and argon gases. The sample set consisted of wafers having thin nickel films with varying thickness.

The diamond seeding process consisted of, first, mixing 1 ml of dimethyl sulfoxide (DMSO), 3 ml of S1813 photoresist and 1 ml of diamond seeds having 5-40 nm diameter and then spinning coating the wafer with the Laurell EDC spin coater at 2500 rpm speed and 1000 rpm acceleration for 25 sec. This blanket seeding method is commonly used by our research group and can produce a nucleation density of approximately  $10^{10}$  cm<sup>-2</sup>. The first set of seeded wafers with a 15 nm thick Ni film were annealed at various temperatures in the tube furnace in the presence of nitrogen atmosphere, while another set of seeded wafers were kept unannealed. The annealing temperature was determined based upon the phases occurring in annealed Ni in the presence of N<sub>2</sub> gas based on the Ni-Si equilibrium phase diagram (Figure 11). The purpose of annealing was to preferentially orient the nano-diamond seeds along the substrate orientation. After annealing, HFCVD diamond was deposited at 1.5 % methane concentration for 3 h for the first stage growth and another 6 h for the second stage growth.

The second set of experiments focused on diamond growth on a seeded Si substrate with 5 nm, 10 nm, 15 nm, and 20 nm Ni modification layers without annealing. The diamond was grown via HFCVD with, again, 1.5 % methane concentration with 2 SLM H<sub>2</sub>, 3 sccm O<sub>2</sub> gas flowed for 3 h. All sample were grown at a chamber pressure of 20.8 Torr., and with a 6 mm sample to wire distance with a substrate temperature of 670 °C as measured by an IR pyrometer. The oriented diamond film was characterized by XRD by comparing the intensity of the diamond peaks. Both parallel beam and Bragg Brentano slit configurations were used to scan the samples at different positions across the wafer using the X-Y stage. The surface roughness and the thickness of the deposited

diamond films were characterized with profilometry. AFM characterized the surface morphology of the films with different scan areas, and SEM images were taken at 10 kV and 0.34 nA. The quality of the diamond films and the presence of non-diamond carbon graphitic phases were characterized by Raman spectroscopy and EDS.

## IV. RESULTS

### 4.1. Diamond growth on annealed nickel thin films

#### 4.1.1. Nickel film characterization

Following Ni film deposition, the thickness and roughness were characterized with ellipsometry and x-ray reflectivity (XRR). The results for the Ni films on Si (111) are summarized in Table 4.

**Table 4.** Thickness and roughness measurements for Ni thin film on Si (111)

Samples	Ellipsometry Results		XRR results		
	Thickness (nm)	Roughness (nm)	Thickness (nm)	Roughness (nm)	Fitted Density (g/cm <sup>3</sup> )
1	4.28±0.28	0.65±0.12	4.96±0.03	0.93	8.56
2	8.81±0.52	0.57±0.18	8.73±0.05	0.34	8.68
3	14.17±0.32	0.30±0.10	12.89±0.03	0.61	8.89
4	16.82±0.26	0.45±0.08	18.25±0.02	0.70	8.81

The spectroscopic ellipsometry measurements were made at two angles of incidence (55° and 65°). The thickness and roughness measured from ellipsometry and XRR generally agree. The measured optical constant value from ellipsometry for Ni is found to be close to the standard value (n=1.97 & k=3.84) [58], and low mean square error (MSE) indicates the data measurement to be plausible and accurate. The variable angle spectroscopic measurement (VASE) and optical constant curve from the ellipsometry measurements are shown in Figures 25 and 26, respectively.

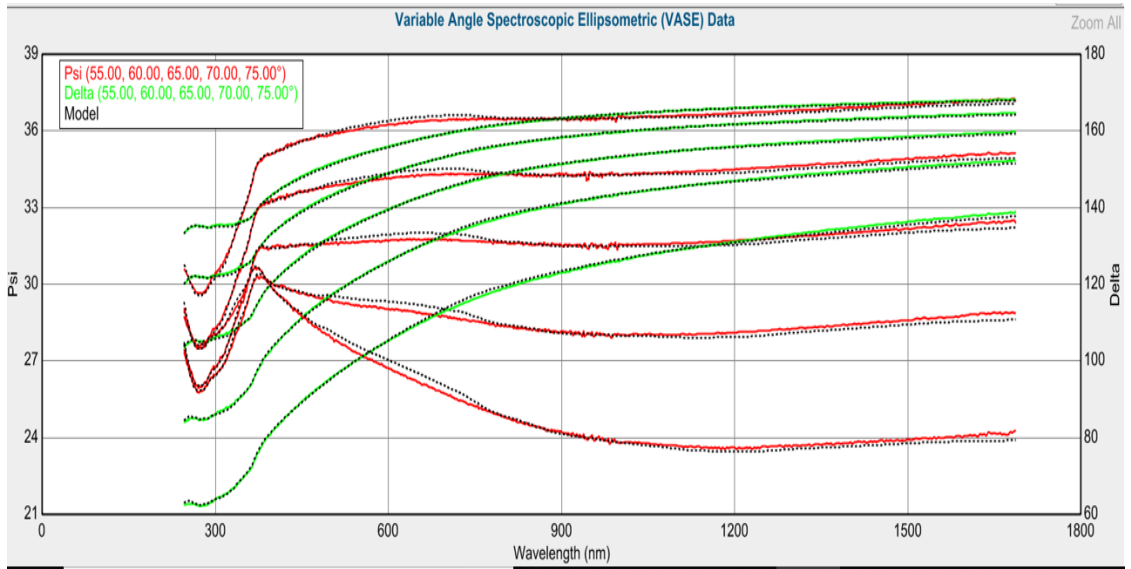


**Figure 25.** Spectroscopic Results for Nickel thin film: The Variable angle spectroscopic Ellipsometry (VASE) data from ellipsometry measurement of thin nickel film on Silicon Substrate.

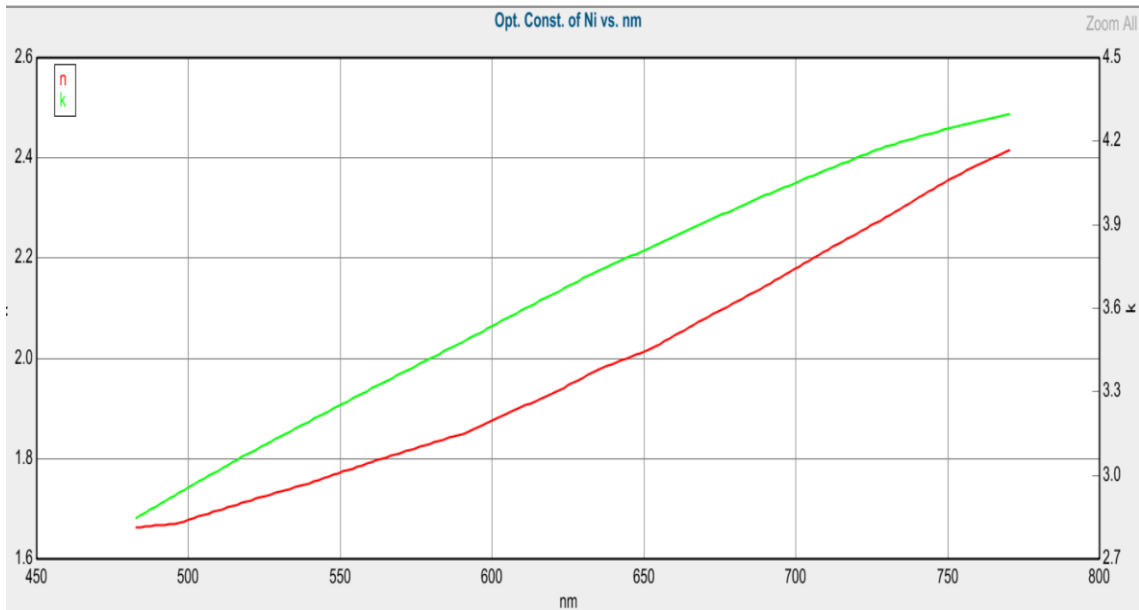


**Figure 26.** Optical constant results for Nickel film from ellipsometer; The optical constants of nickel film (15nm Nickel film on Si substrate) measured from Ellipsometry.

#### 4.1.2. Nickel nanodots array and distributions

AFM images in Figure 27 shows the nickel nanodots self-aggregation on silicon substrates creating as-deposited nickel layers with different thickness after conventional annealing at 800°C for 30 minutes in the presence of N<sub>2</sub> gas. The array patterns of nanoparticles were affected by the thickness of nickel films at the given annealing temperature. The average diameter of the nanodots become larger, and the average distance between adjacent nanodots was increased while their density was reduced with increasing nickel film thickness. In the case of thicker nickel films, the island becomes bigger, and the correlation distance becomes larger due to the nickel nanoclusters merging, thus reducing the density.

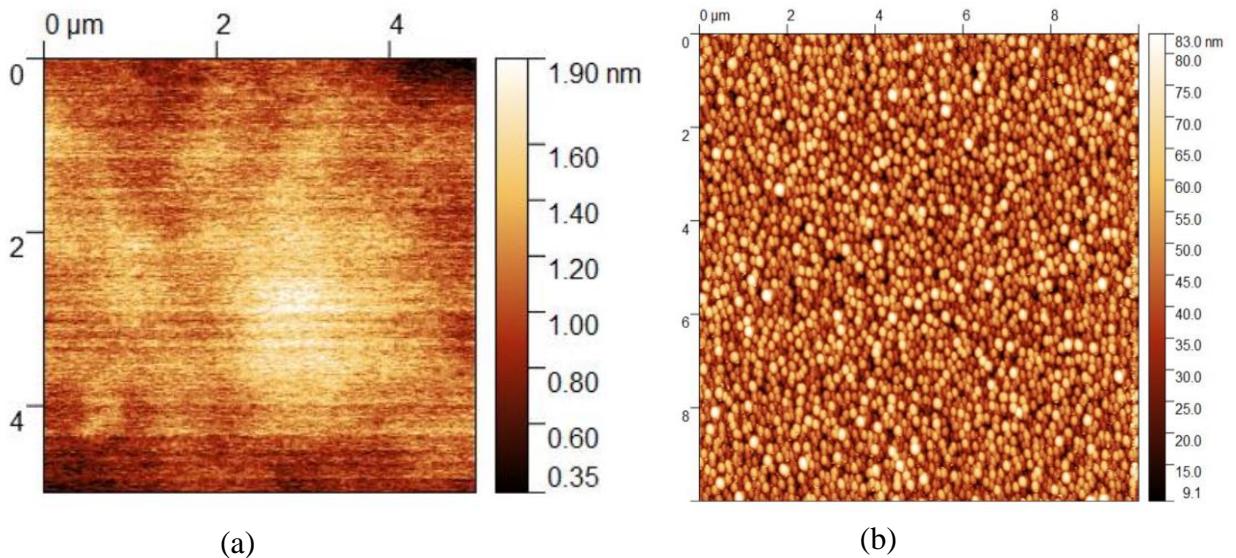


**Figure 27.** AFM images (5μm×5μm) scan for 5 nm nickel thin film on Silicon, a) Before annealing and b) After annealing.

The effect of annealing time on the size and density of the nanodots was also studied by annealing the Ni films at various temperature and time. For higher annealing temperature and time (1000°C for 30 min), the Ni films initially break into larger Ni strips and gradually achieves a spherical shape as shown in Figure 29. Also, the small Ni nanodots eventually self-aggregate, enlarging their average diameter as the annealing time increases to 1h. The reason for this is that a short annealing duration leads to an insufficient self-aggregation of the Ni film and, therefore, unevenly sized nanodots are formed [16,59]. On the contrary, with increasing annealing time, the aggregation of the Ni film can occur, resulting in a fusion of small nanodots into larger ones [16]. In this way, Ni nanodots with uniform size and a regular spherical shape are easily obtained.

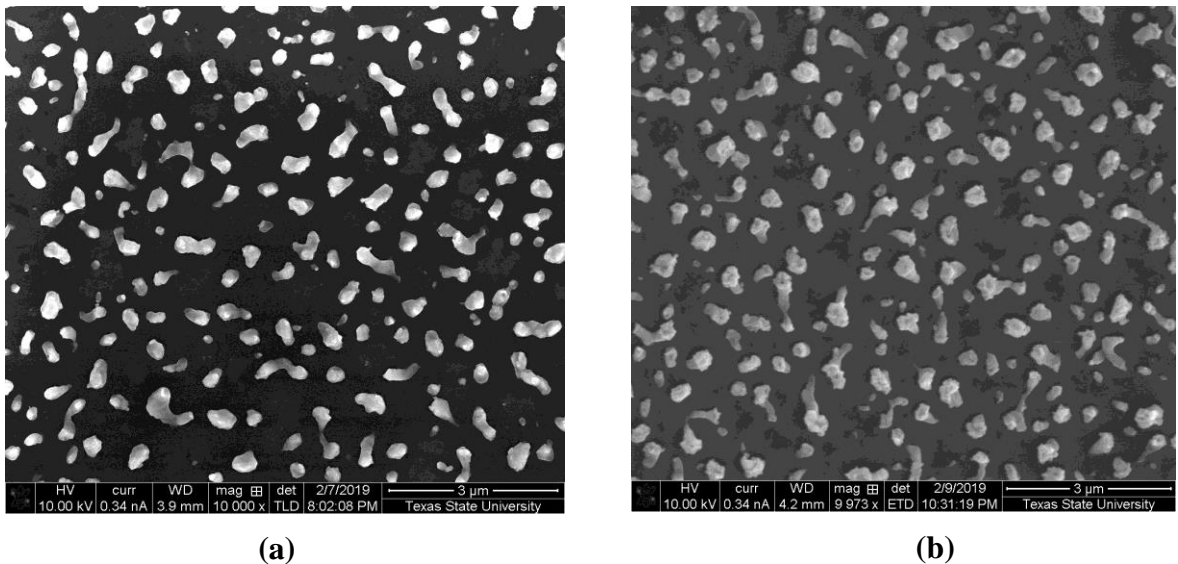
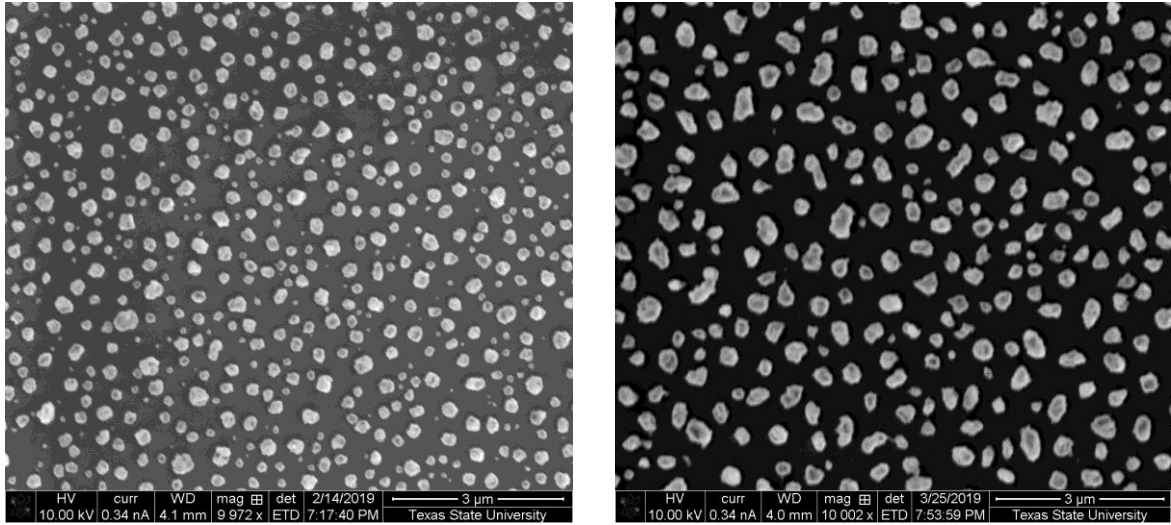


**Figure 28.** SEM images for Ni nanodots (15 nm Ni film on Si) annealed at, a) 600°C for 30 min and b) 600°C for 1 h, in N<sub>2</sub> atmosphere.



a)

b)

**Figure 29.** SEM images for Ni nanodots (15 nm Ni film on Si) annealed at, (a) 1000°C for 30 min, and b) 1000°C for 1 h, in N<sub>2</sub> atmosphere.

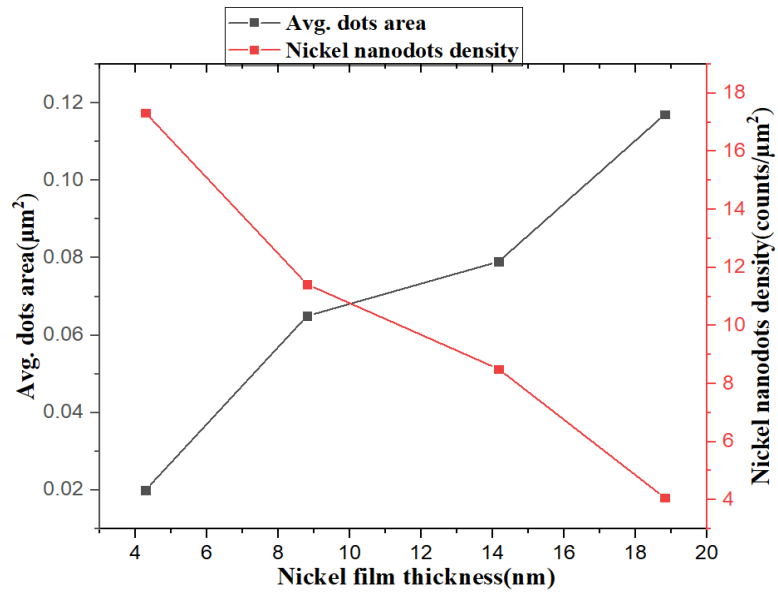
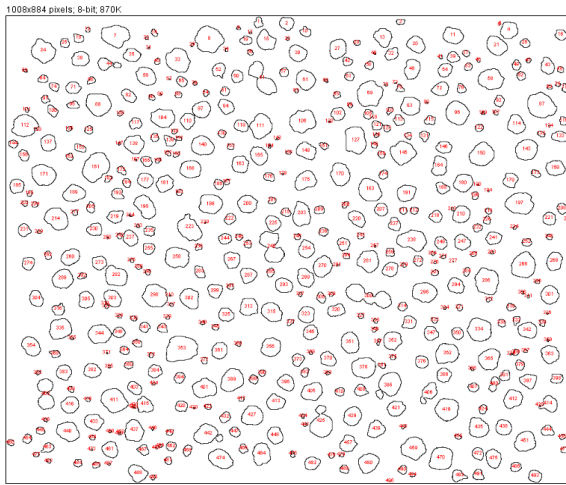
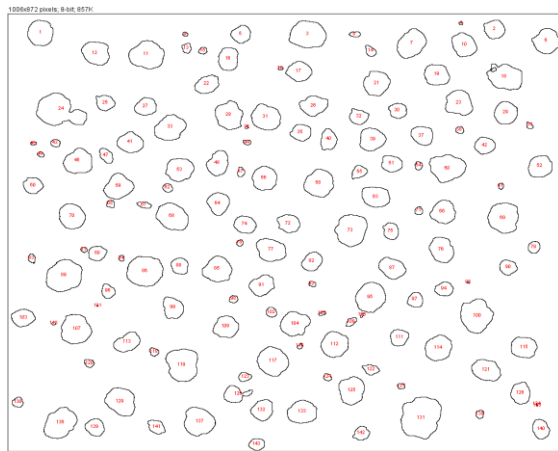
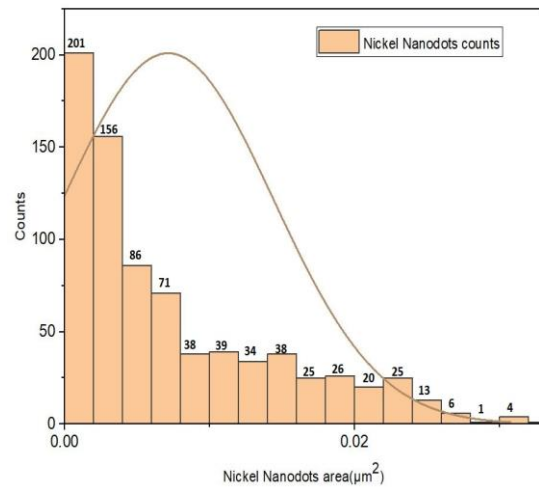


**Figure 30.** Nickel nanodots density and area distribution with nickel film thickness.

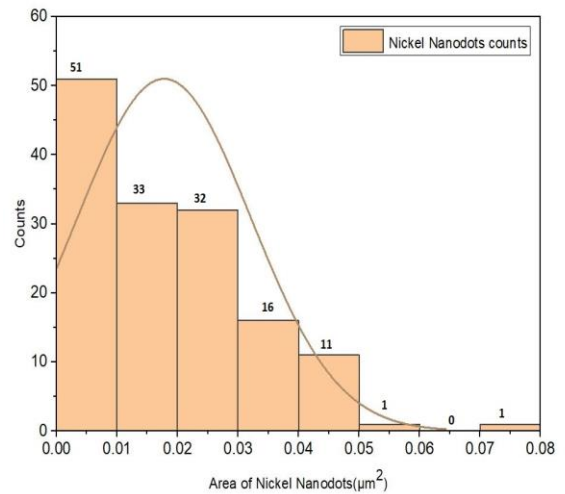
The distribution of Ni nanodots after annealing the various Ni film thickness samples at 800°C for 30 min in N<sub>2</sub> atmosphere was analyzed by Fiji Image J software. The density and area of Ni nanodots with Ni thickness is shown in Figure 30. It is found that the density of Ni nanodots increases with decreasing Ni thickness. The distribution of nanodots on Si (111) for various Ni thicknesses is shown in Figure 31.

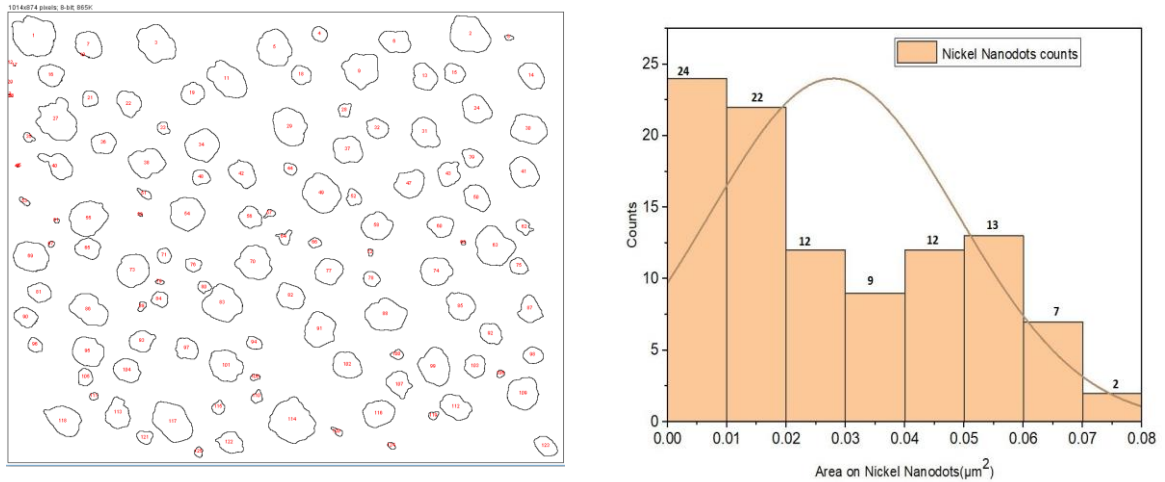


**a)**

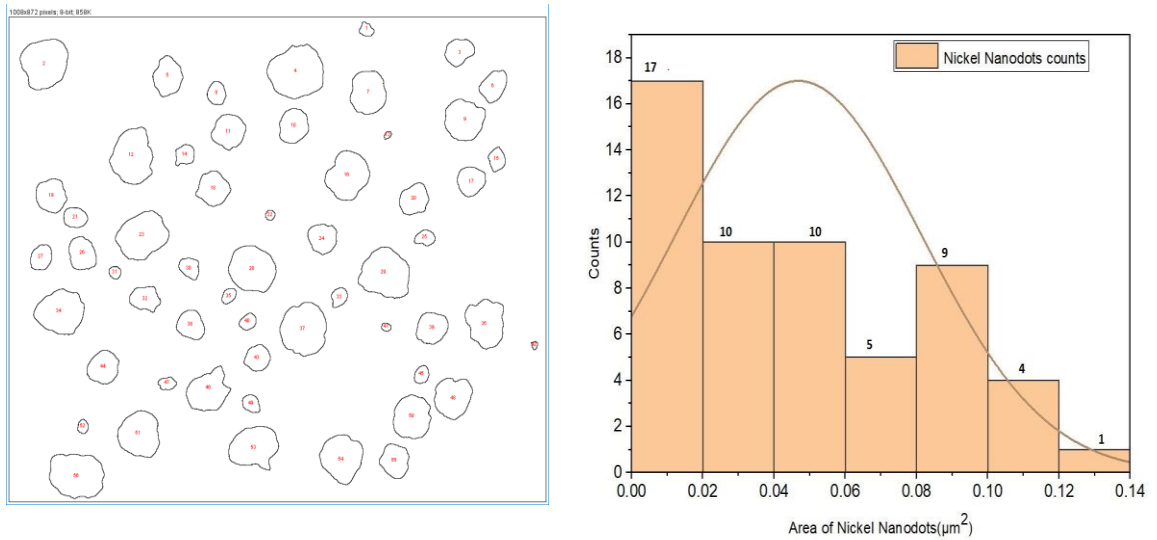


**b)**





c)



d)

**Figure 31.** Distribution of Ni nanodots on a Si(111) substrate; The distribution of Ni nanodots at different Ni thicknesses (a) 5nm Ni (b) 10nm Ni (c) 15nm Ni and (d) 20nm Ni, after annealing at 800 °C for 30 min in presence of N<sub>2</sub> gas characterized through Fiji Image J software.

In general, the solid-state aggregation of a thin metal film is a phenomenon allowing the film aggregation to spontaneously form specifically shaped particles when reaching a certain temperature below the melting point [16]. It has been found that the density of the Ni nanoparticles gradually decreased but then reversed with increasing

annealing temperature due to migration of Ni atoms into the substrate surface enhanced by a higher temperature. I.e., Ni atoms aggregated on the surface of large nanoparticles thereby reducing the interfacial energy and achieving the minimum free energy [16] [22].

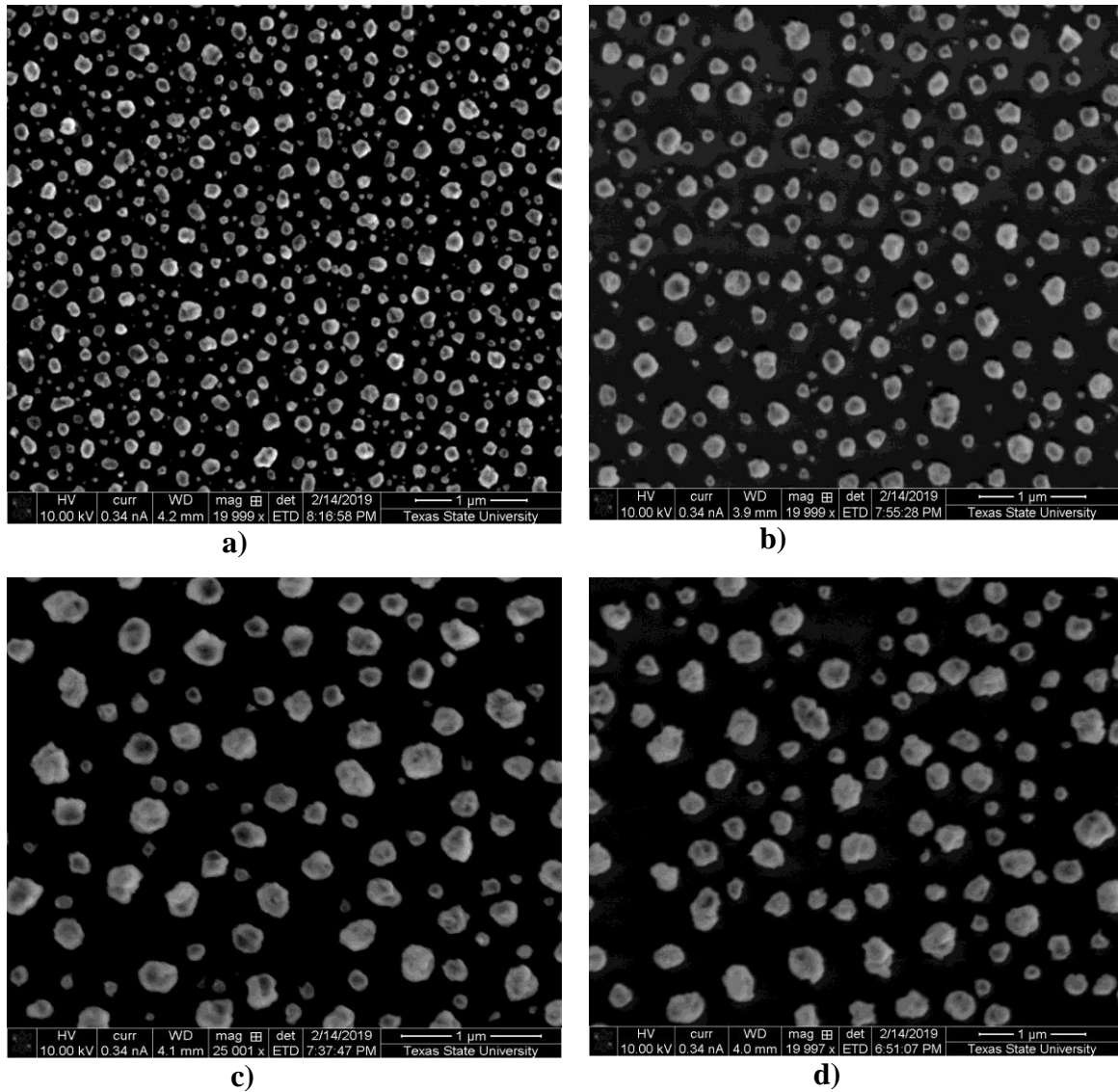


**Figure 32.** SEM images for Ni nanodots formed on Si substrate; The figure shows Ni nanodots SEM images for different Ni film thickness a) 5nm Ni, b) 10nm Ni, c) 15nm Ni and d) 20nm Ni, on Si(111) substrate, when annealed at 800°C for 30 min in N<sub>2</sub> atmosphere.

Similarly, the shape and size of nanodots depend upon the thickness of the surface oxide layer between the Ni and Si substrate [22]. If we consider a thin barrier oxide layer between the Ni and Si, then the temperature plays a significant role in maintaining the size and distribution of nanodots due to the difference in thermal conductivity of Si and SiO<sub>2</sub>. The SEM images for Ni nanodots formed for different thickness at 800 °C for 30 min is shown in Figure 32.

#### **4.1.3. Phases changes in Nickel thin films by annealing**

The study of solid state phase change through annealing Ni thin films on silicon depends upon the temperature, as indicated by the Ni-Si phase diagram in Figure 11. X-ray diffraction patterns are shown in Figure 33 for a 15 nm Ni film grown on Si (111). The XRD scans reveal strong Ni (220) peaks at 76.08° and Si (111) peaks at 28.47° for unannealed and annealed films. The XRD patterns for the annealed film at 600 °C and 800 °C for 30 min in the presence of nitrogen atmosphere indicate the formation of nickel silicide phases as revealed by a NiSi peak, as well as Ni rich silicon phase, Ni<sub>3</sub>Si, for the sample annealed for 30 min at 600 °C. The reaction between Ni and Si forms a Ni-rich silicide phase, and then further diffusion on the silicon surface causes additional silicide phases [25]. At very low temperature, the diffusion reaction rate between the Ni and Si is slow, resulting in the formation of di-nickel silicide (Ni<sub>2</sub>Si) at the interface between the Ni and Si [25,60]. Higher annealing temperature will transform Ni<sub>2</sub>Si into NiSi phase [25]. The NiSi phase is stable for the sample annealed for 600 °C for 30 min, as shown in the XRD data.

The Ni-Si reaction at 800 °C and 30 min produced the epitaxial growth of the NiSi<sub>2</sub> phase on Si. The NiSi<sub>2</sub> phase is stable for this temperature and the strong NiSi<sub>2</sub>

(220) peak at  $76.08^\circ$  represents the film texture along that direction. Di-nickel silicide ( $\text{Ni}_2\text{Si}$ ), nickel monosilicide ( $\text{NiSi}$ ) and nickel di-silicide ( $\text{NiSi}_2$ ) are formed at the progressively higher annealing temperature [25].  $\text{NiSi}_2$  grows epitaxially on Si due to their close lattice parameters ( $a_{\text{silicon}}=5.43\text{\AA}$  &  $a_{\text{NiSi}_2}=5.47\text{\AA}$ ), and the crystals have the same texture as Ni film on Si [61].

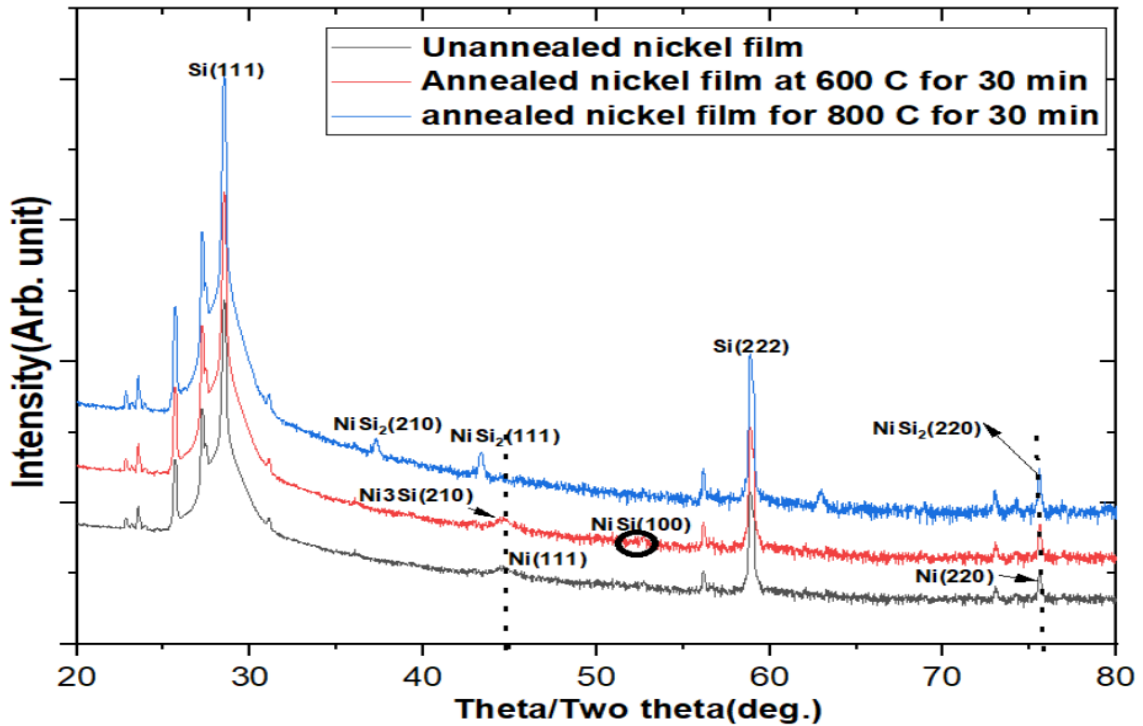


**Figure 33.** XRD analysis of 15 nm Ni film before and after annealing at various temperature.

The nickel silicide phases on Si and secondary compounds formed during annealing were characterized by Raman spectroscopy. The Raman spectra were taken with a 532 nm laser, a selective filter of 10% in the detection channel, and a cooled silicon 2D CCD array detector. The Raman spectrum of the unannealed 15 nm Ni sample exhibits only Si lines at  $301$  and  $520\text{ cm}^{-1}$  and a silicon carbide line at  $950\text{ cm}^{-1}$ . Figure 34

shows the Raman spectrum for both unannealed and annealed 15nm Ni on Si at 800 °C for 30 min. After annealing, the 301 cm<sup>-1</sup> Si peak intensity increases. This is due to an associated acoustic vibration of Ni and Si at the interface. For the annealed Ni film, the lines at 217 and 255 cm<sup>-1</sup> are interpreted as being associated with NiSi. The three bands of Raman spectrum at 430, 615, and 670 cm<sup>-1</sup> represent the lines for NiSi<sub>2</sub>.

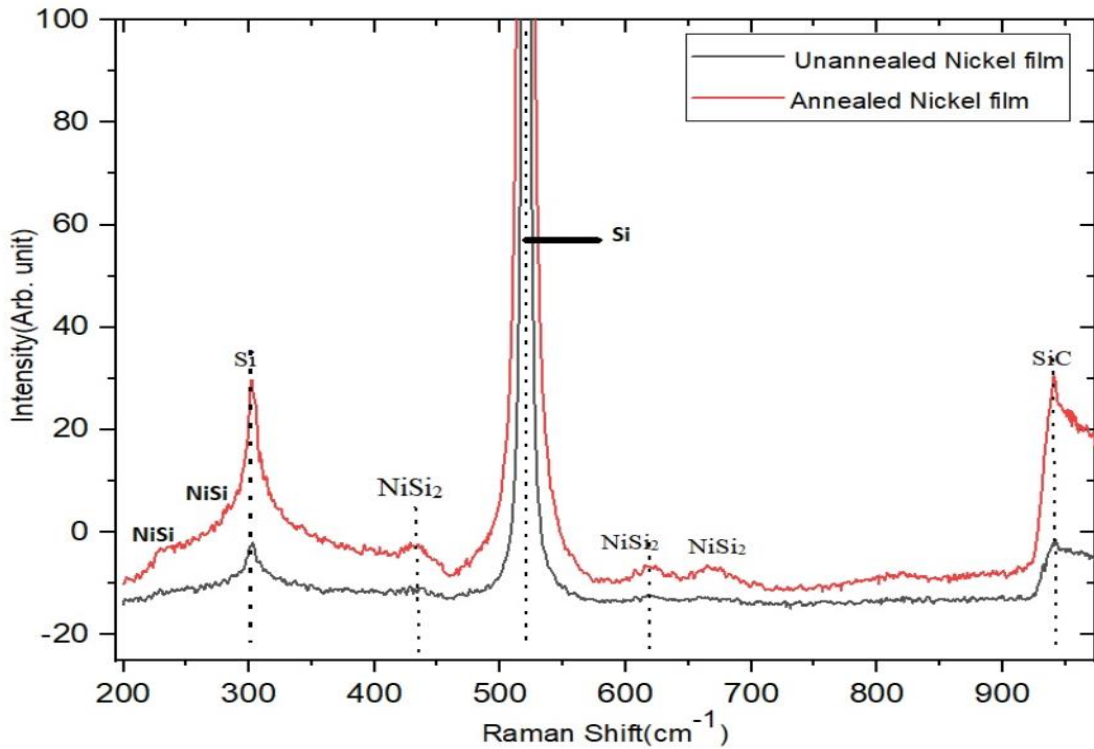


**Figure 34.** Raman spectrum of 15nm nickel film before and after annealing at 800 °C in N<sub>2</sub> gas atmosphere.

Based upon the data of annealed Ni thin films on Si (111), we found NiSi<sub>2</sub> is the stable phase when the annealing temperature is 800 °C. NiSi<sub>2</sub> has a molten phase state at 983 °C from the phase diagram (Figure 11). Therefore, we fixed the annealing temperature for diamond seeded wafers based on the molten phase state of Ni and Si from the equilibrium phase diagram.

#### 4.1.4. Diamond growth and characterization

The distribution and area of Ni nanodots for the 15 nm Ni film on Si (111) are more uniform than the other Ni thicknesses investigated, when annealed at 800 °C for 30 min in N<sub>2</sub>. It is expected that the uniformly distributed nanodots will help to crystallographically orient the diamond seeds due to the stress developed between the Ni nanodot surface and diamond seed. Thus, Ni films with 15 nm thickness on Si (111) were chosen for diamond seeding and growth studies. The seeded wafers with the 15 nm Ni modification layer were annealed in a tube furnace at different temperatures. One wafer was annealed at 800 °C for 30 min, while the other was annealed at 800 °C for 30 min and 920 °C for 1min in nitrogen atmosphere. The SEM surface morphologies of the annealed diamond seeded wafers at the two different temperatures are shown in Figure 35.

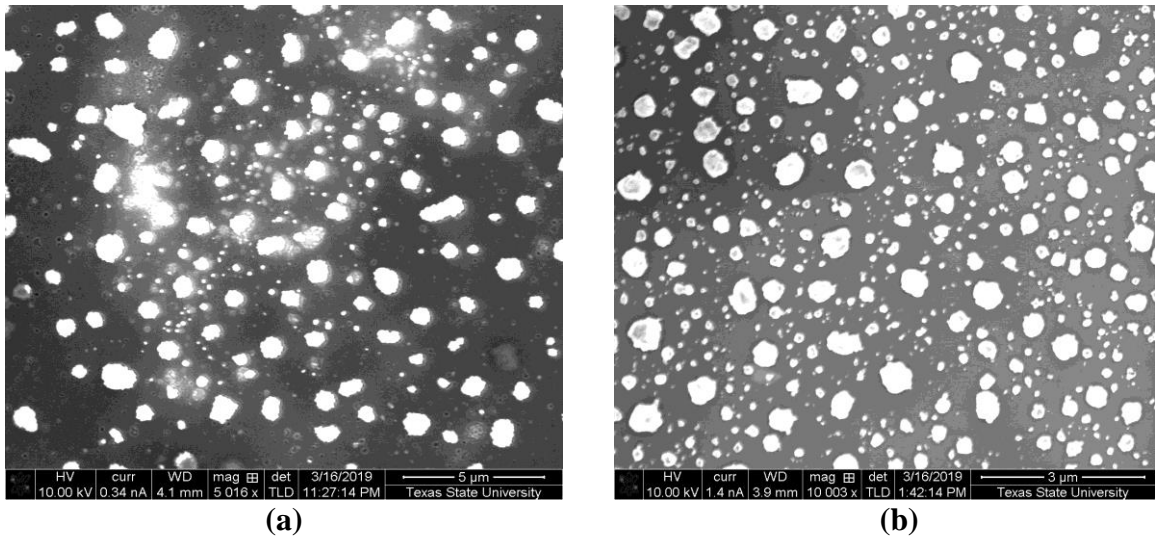
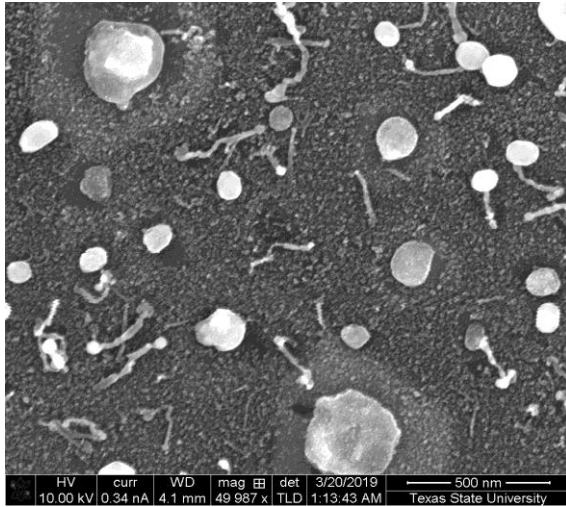


**Figure 35.** SEM images for annealed diamond seeded wafer at (a) 800 °C for 30 min, and (b) 800 °C for 30 min + 920 °C for 1 min.

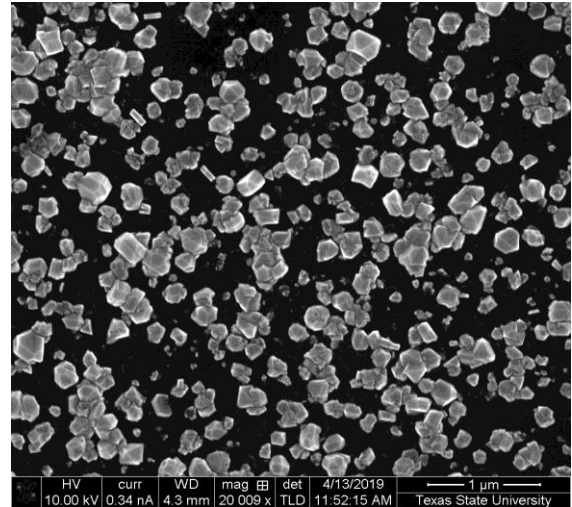
The SEM images shows the distribution of nickel nanodots on the annealed seeded wafers and we can expect the stress between the Ni nanodots, and diamond seeds helps the distributions of diamond seeds and their orientation, for better nucleation of diamond films during diamond growth. After annealing, HFCVD diamond films were grown with 1.5% methane concentration with 2 LPM H<sub>2</sub>, 3 sccm O<sub>2</sub> gas flowed for 3 h for the first stage, followed by an additional 6 h for the second stage. The diamond nucleation, growth, and coverage of diamond nuclei were characterized with SEM, AFM, and surface profilometry. The oriented diamond nuclei and diamond films were characterized with XRD and the quality of the diamond films was characterized via Raman Spectroscopy.

#### **4.1.5. Nucleation and growth of diamond film**

The diamond nucleation density was low for both annealed wafers, as well as on silicon, following 3 hours growth as shown in Figures 36 and 37. A diamond ‘cauliflower’ texture is obtained on the sample annealed for two steps while there is well faceted diamond islands with the one step annealed sample, due to the beneficial formation of NiSi<sub>2</sub>. The low diamond nucleation density on these samples (even compared to diamond directly on silicon, Figure 36(a) is due to poor adhesion on nickel silicide. The poor adhesion of diamond on the nickel silicide surface is due to the difference in thermal expansion coefficients (linear thermal expansion coefficient of diamond and nickel di-silicide are  $\sim 10^{-6}/^{\circ}\text{C}$  [10] and  $\sim 10 \times 10^{-6}/^{\circ}\text{C}$  at room temperature [62], respectively). Furthermore, the different growth modes of diamond on nickel silicide is due to the depletion of the graphitic surface layer. The faceted diamond growth on silicon-rich NiSi<sub>2</sub> is expected due to the formation of stoichiometric Si<sub>(1-x)</sub>C<sub>(1-x)</sub> phases, which is analogous to the conditions on the silicon substrate surface.

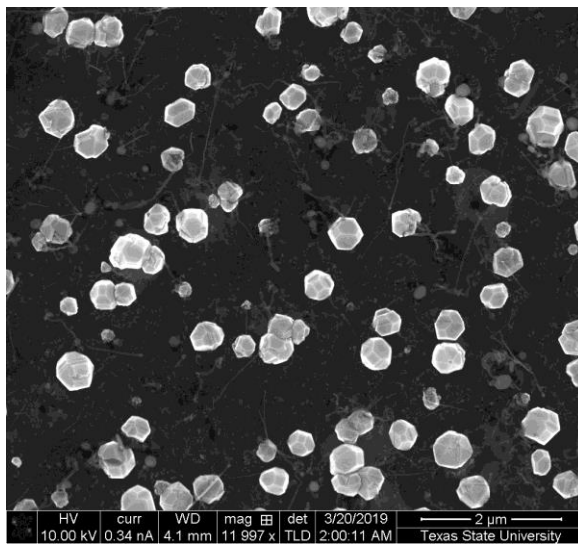


**a)**

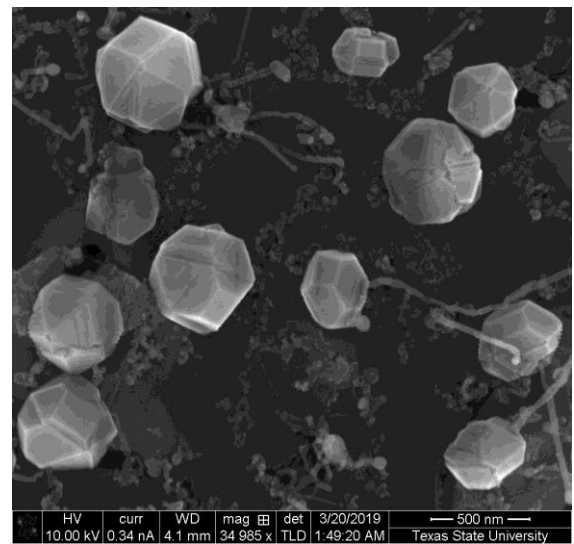


**b)**

**Figure 36.** SEM images for diamond (a) ‘cauliflower’ texture in the annealed Ni film on Si (111) for 800 °C for 30 min + 920 °C for 1 min. and (b) diamond seeded growth directly on Si (111).



**a)**



**b)**

**Figure 37.** SEM images for 3 h diamond growth on the annealed Ni thin film on Si (111) at 800 °C for 30 min.

Due to the poor diamond nucleation density on the annealed samples, coalesced diamond films did not form within the 3 h growth run and, furthermore, the texture analysis was complicated. Therefore, the sample was reloaded in the HFCVD diamond system for an additional 6 h growth. Highly coalesced diamond films with well faceted large grains are formed on the sample with one-step anneal. However, the diamond nuclei did not coalesce on the two-step annealed sample as seen in Figure 38. The poor nucleation of the diamond film on the two-step annealed sample is believed to be due to high heat accumulation at the nickel silicide nanodots during the high-temperature anneal resulting in most of the diamond seeds being dissolved into the nickel silicide, as shown in Figure 38(b).

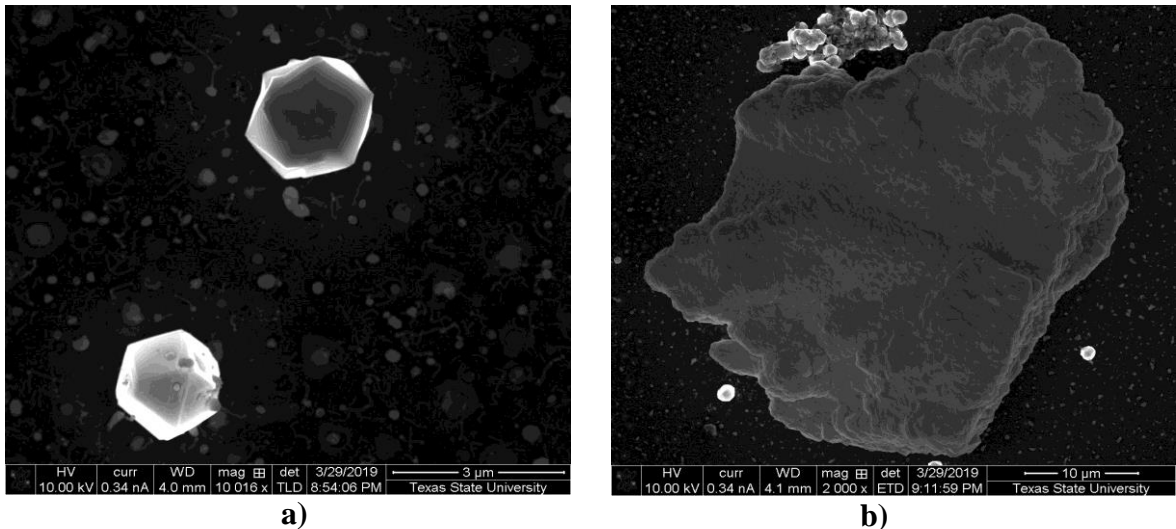


**Figure 38.** SEM images of diamond growth on the two-step (3 + 6 h) annealed sample.

Figure 39 shows the  $\Theta$ - $2\Theta$  x-ray diffraction pattern of the one-step annealed sample after a total of 9 h diamond growth. The data indicate diamond (111) and (220) peaks at  $43.9^\circ$  and  $75.6^\circ$ , respectively. The diamond film crystallographic texture was characterized through XRD by determining the degree of texture (R) from the integrated

diamond peak intensities. The degree of texture for the diamond film is  $R = I_{(111)}/I_{(220)} = 5.8$  (15 mm from wafer center), 7.2 (30 mm from wafer center) and 3.6 (45 mm from wafer center). The texture of the diamond sample was analyzed by comparing the diffracted peak intensities to a randomly oriented diamond crystal. Specifically, the powder diffraction pattern of diamond from the American Society of Testing Materials (ASTM 6-0675) indicates  $I_{(111)}/I_{(220)} = 4$  for a randomly oriented sample. From SEM images, we found that most crystallites in the fine grain diamond film at the sample center and middle regions are oriented along the (111) direction while most crystallites with medium grain diamond at the edge of sample are oriented along the (220) direction. The SEM images for diamond surface grown on 15nm Ni film at 45mm from wafer center is shown in Figure 43.

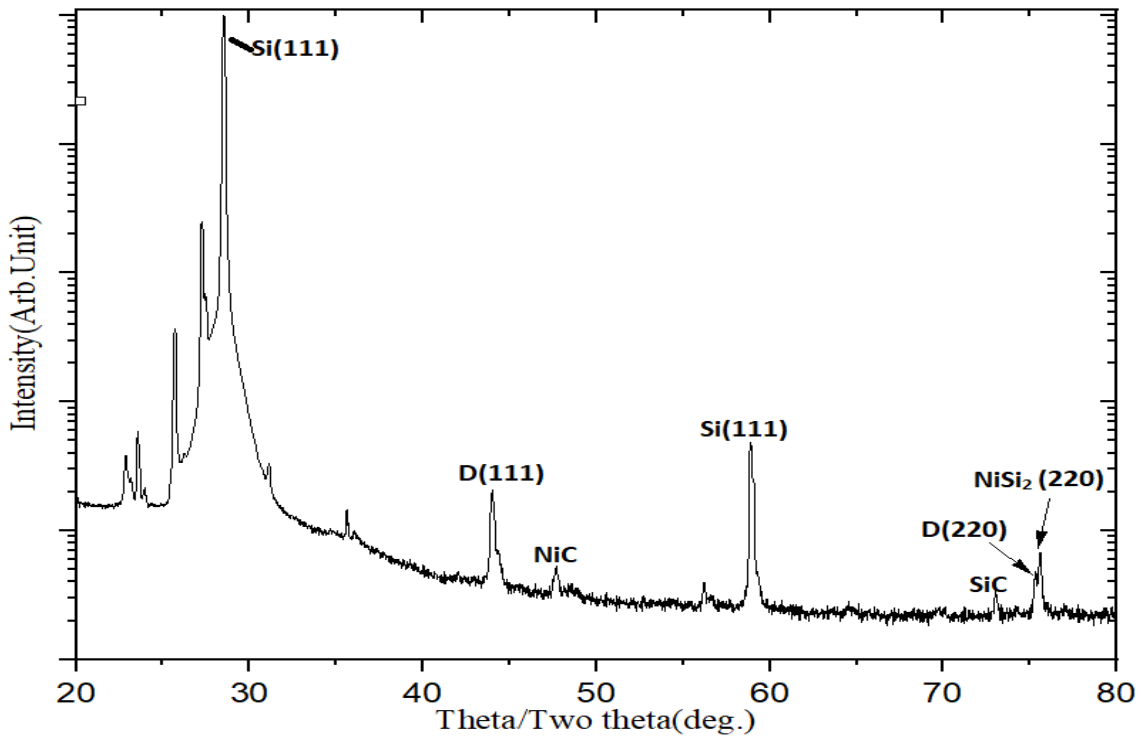


**Figure 39.** Medium resolution parallel beam XRD scan for 9 h diamond growth on annealed Ni film on Si (111) at 800 °C for 30 min.

The difference in texture at different sample positions is due to variations in the annealing temperature in the three-zone tube furnace during annealing of the seeded wafer before diamond growth. Due to a lower temperature at the wafer edge, diamond seeds remain at the surface of the Ni nanodots with random orientations. During diamond growth, the Ni-C eutectic phase is formed, which grows epitaxially. Diamond seeds move on the grain boundaries of nickel carbide and orient along the (220) direction due to stress produced at the grain boundaries thereby resulting in less diamond (111) texture at the sample edge. Furthermore, the (111) oriented diamond film in the center and middle regions is due to partial dissolution of the seeded diamond fragments on the Ni lattice. These partially oriented diamond particles are then reoriented into alignment with the orientation of the surrounding Si substrate due to the interaction between the two lattices.

#### **4.1.6. Quality of diamond film**

A representative Raman spectrum is shown in Figure 40 and confirms that the diamond peak is sharp with a low FWHM and the small non-diamond peak indicates quality of diamond films in terms of grain size and its purity. Furthermore, the non-diamond carbon (NDC) percentage of the sample is low, at 14%. The calculated area under the curve using the Lorentzian curve fitting approach was used to determine the NDC content, represented in Figure 41. The Raman spectrum of the sample contains one Raman peak centered at  $1332\text{ cm}^{-1}$  and a broader band centered at  $1550\text{ cm}^{-1}$ . The sharp peak at  $1332\text{ cm}^{-1}$  is characteristic of  $\text{sp}^3$  bonded carbon, i.e., the diamond form. The broad peak at  $1550\text{ cm}^{-1}$  represents the  $\text{sp}^2$  bonded carbon, i.e., NDC. The suppression of graphitic content is based on the Ni-C eutectic phase forming when the annealed Ni sample is subjected to the HFCVD environment. Ni absorbs carbon (and hydrogen) and

forms nucleating sites for the diamond growth resulting in the preferential formation of  $sp^3$  bonded carbon and suppression of the  $sp^2$  carbon bond.

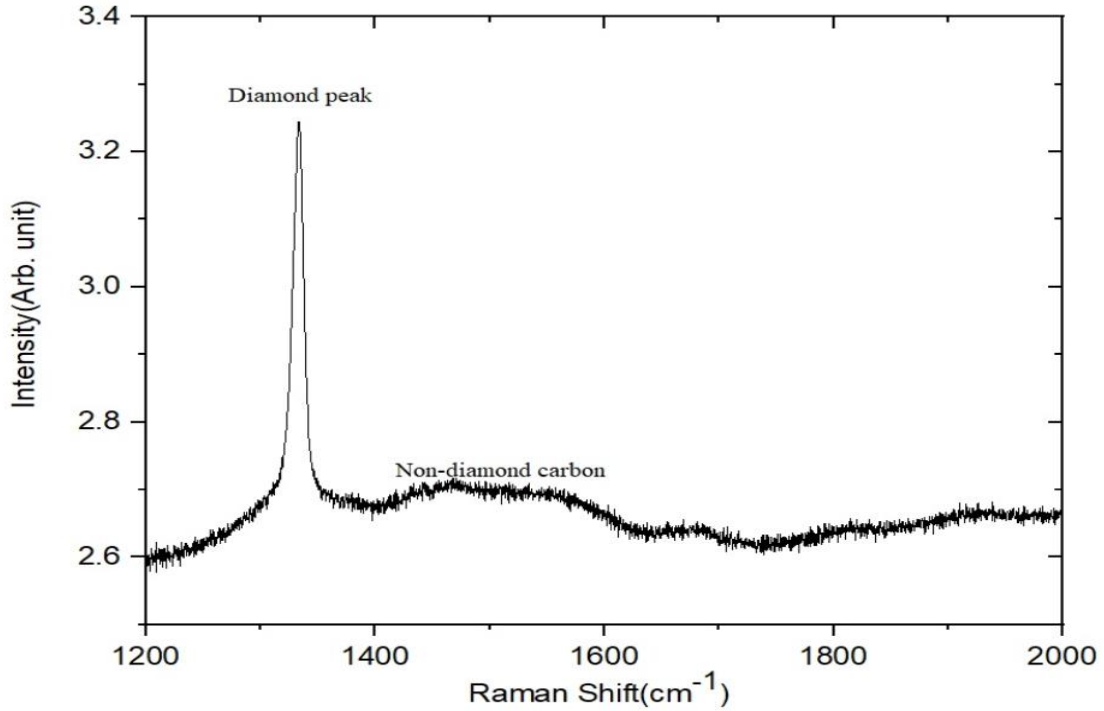


**Figure 40.** Raman spectra for diamond grown on the one-step annealed Ni thin film.

Additionally, lower NDC content can be due to highly coalesced oriented diamond grains with 2-5  $\mu\text{m}$  diameter and, thus, fewer grains boundaries. The full width at half maximum (FWHM) of the diamond peak at  $1332\text{ cm}^{-1}$  is  $8.94\text{ cm}^{-1}$  indicating the low defect density of the diamond film. The surface roughness and morphology of the diamond were characterized by SEM and AFM. The diamond film grown on the one-step annealed Ni has low surface roughness due to significant grain coalescence. The average roughness measured by surface profilometry on the sample is  $(78.73 \pm 4.03)\text{ nm}$  with an

average AFM RMS roughness of  $(71.50 \pm 2.15)$  nm. The SEM and AFM scans for the diamond sample is shown in Figures 42 and 43, respectively.

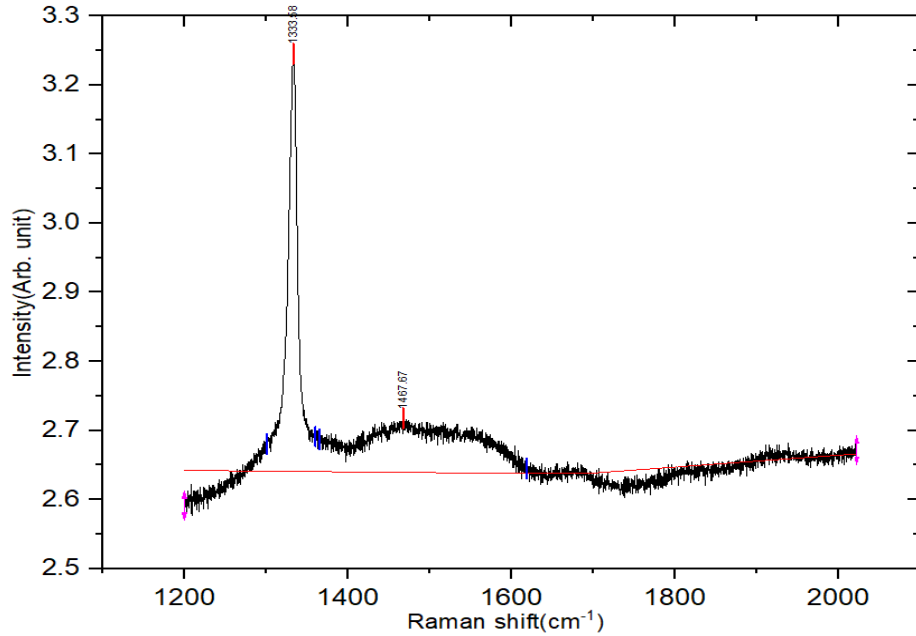


**Figure 41.** Integrated curve fitting, with baseline (red), used to calculate the peak areas for diamond and NDC.

In summary, a seeding and multistep deposition process has been developed to nucleate and grow oriented diamond films by pre-annealing 15 nm thick Ni films on Si (111) at 800 °C for 30 mins. The oriented diamond film is due to the preferential orientation of the diamond seeds by the production of stress between the diamond seeds and nickel silicide nanodots resulting from thermal annealing. While many of the diamond seed partially dissolve into the nickel silicide, those that remain coordinate with the nickel silicide lattice, which has the same lattice constant as silicon, and finally diamond grows on the undissolved seeds oriented with the substrate. The quality of the diamond film is improved in terms of crystal size due to large grains and low NDC

content. Furthermore, better quality diamond is due to nickel silicide nanodots which act to suppress the formation of graphitic carbon by the development of intermediate nickel carbide, which enhances the  $sp^3$  bonded carbon growth. Hence, nickel carbide acts to absorb non-diamond carbon, orient the diamond seed, and create an environment whereby the diamond nuclei remain at the surface resulting in the growth of high crystalline textured diamond films.

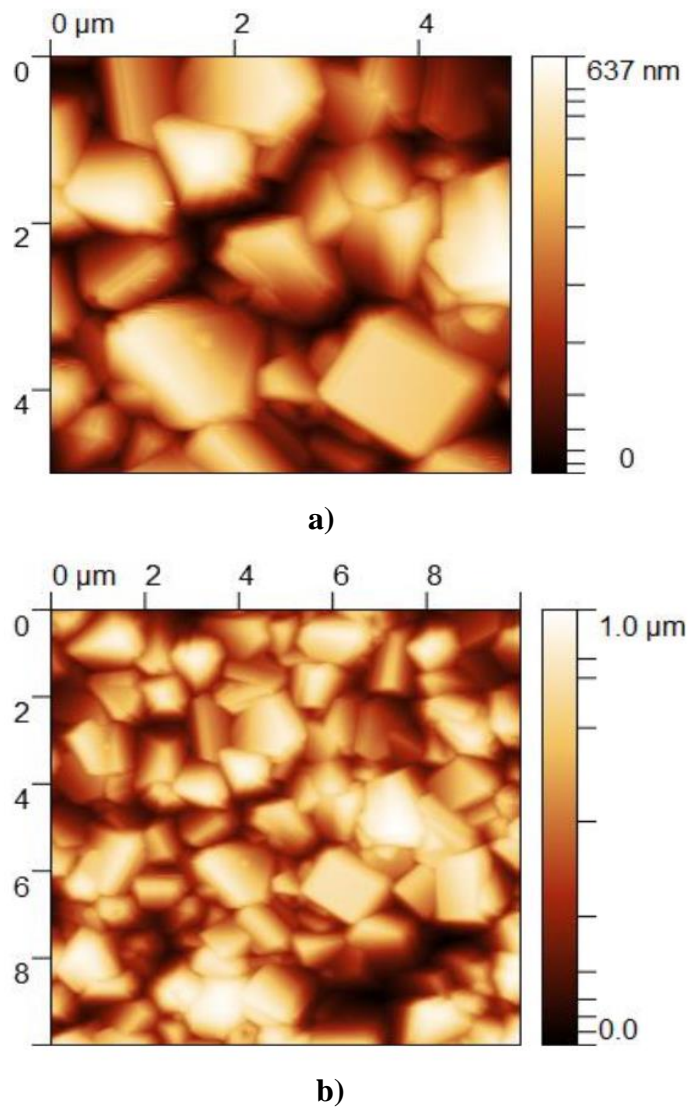


**Figure 42.** AFM images of (a)  $5 \mu\text{m} \times 5 \mu\text{m}$  and (b)  $10 \mu\text{m} \times 10 \mu\text{m}$ , of the diamond film at 45 mm from the center of the wafer.

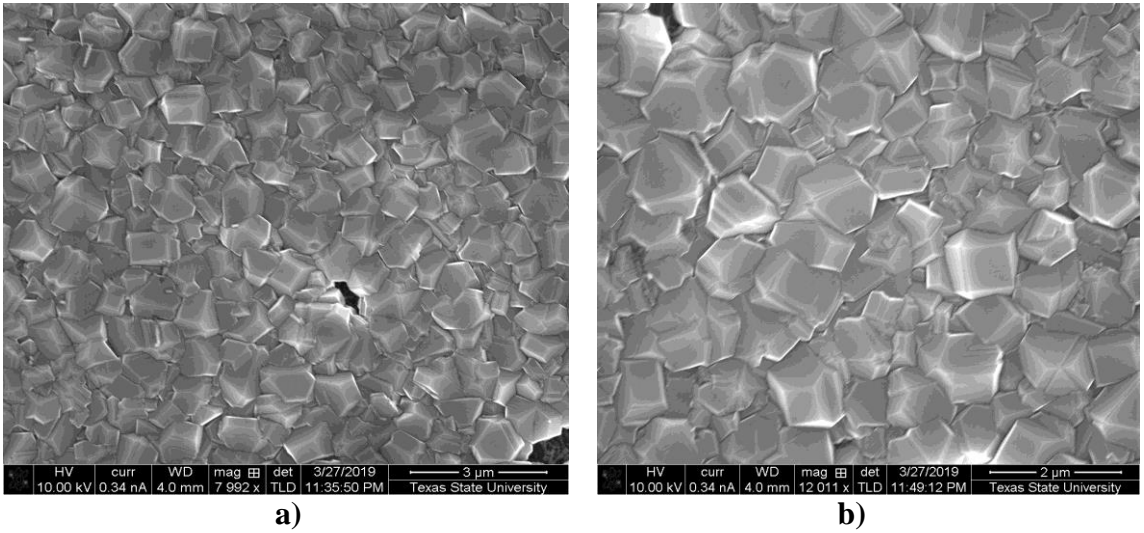


**Figure 43.** SEM images of the diamond surface grown on 15 nm annealed Ni for 9 h at 45 mm from the center of the wafer.

However, there are still challenges associated with the thermal annealing process. Due to high heat accumulation at the nickel silicide dots, the dots may melt due to the diamond nano-seeds dissolving into the nickel nanodots, which create poor nucleation conditions for the diamond. The wafers subjected to the two-step annealing process exhibited such problems not allowing for coalesced diamond films. Thus, the focus of the next study is novel approaches for heat treating the diamond seeded Ni thin film.

## **4.2. Diamond growth on nickel modification layer without annealing**

### **4.2.1. Substrate pre-treatment and diamond deposition**

Analogous HFCVD conditions from the previous study were employed for diamond deposition in the present study. Specifically, the deposition conditions were 1.5% methane with 2 LPM H<sub>2</sub>, 3 sccm O<sub>2</sub> and 3 h growth time. The substrate temperature was 670 °C. P-type Si (111) was used to deposit Ni films with thicknesses of 5, 10, 15 and 20 nm. The characterization processes for this study were, likewise, analogous to the previous study. Thickness and roughness were characterized by ellipsometry, AFM, and profilometry. The Ni-coated substrates were solvent cleaned with acetone, methanol, and isopropanol. The cleaned substrates were seeded by the same photolithography process employed in the first study, discussed previously.

### **4.2.2. Characterization**

Film morphology was characterized by field emission SEM at 10 kV and 0.34 nA. Microstructure and diamond quality were characterized with Raman spectroscopy at room temperature using a 532 nm laser scanning from 450-2000 cm<sup>-1</sup>. Before Raman analysis, the instrument was calibrated using a reference silicon substrate. XRD using CuK<sub>α</sub> radiation at a wavelength of 0.154nm was performed to study the phase and texture of the films using the Rigaku Smart lab diffractometer.

### 4.2.3. Diamond nucleation and crystal development

In the HFCVD diamond process, the nucleation of diamond depends upon the availability of diamond seeds on the substrate surface. The seeds are supplied to the Si substrate by blanket seeding techniques and are the initiation points for subsequent diamond nucleation and growth. The SEM images after 3 h diamond growth is given in Figure 45 for (a) no Ni, and (b) – (e) 5, 10, 15, and 20 nm Ni modified layers, respectively. There is a significant increase in diamond grains size with increased Ni film thickness.

It can also be seen that nucleation of diamond films on the pre-seeded silicon substrate with 20 nm nickel modification layer forms Nano diamond nuclei with a low crystalline structure. This type of diamond growth is typically referred to as ‘Cauliflower’ or ‘Ballas-type’ growth morphology. However, diamond growth on the 5, 10, and 15 nm thick Ni modification layers has well faceted diamond grains with sizes ranging from 0.5 to 1.5  $\mu\text{m}$ . Generally, for diamond deposition, due to different surface structure that depend on crystallography, some grains will grow faster than the others. There is no Ni diffusion to the diamond film from the substrate for 5, 10 and 15 nm nickel modification layers but nickel diffuses to the diamond film when it was grown on the 20 nm nickel film as shown in the XRD data in Figure 50. The reason for this is the nickel film was not completely consumed to form nickel carbide alloys during diamond deposition and remains at the surface to diffuse into the diamond film. Diamond nuclei are closer to thermal equilibrium shapes such as octahedral, rhombic dodecahedron, and truncated octahedron pictured by SEM images on Figure 45. The flake grains due to twin crystal is scarce, and the quality improvement is attributed to the nickel modification layers. The

diamond film coalescence and growth rate are also increasing with increasing Ni thickness, which was characterized by surface profilometer.

Compared to the diamond film on Si, all the diamond films on the modified Ni layers exhibit better surface coverage and coalescence. The enhanced diamond nucleation kinetics on the Ni modified layers is conducive to more uniform diamond growth. Raman analysis was performed to investigate the crystalline development of the diamond after 3 h growth. The results are shown in Figure 44.

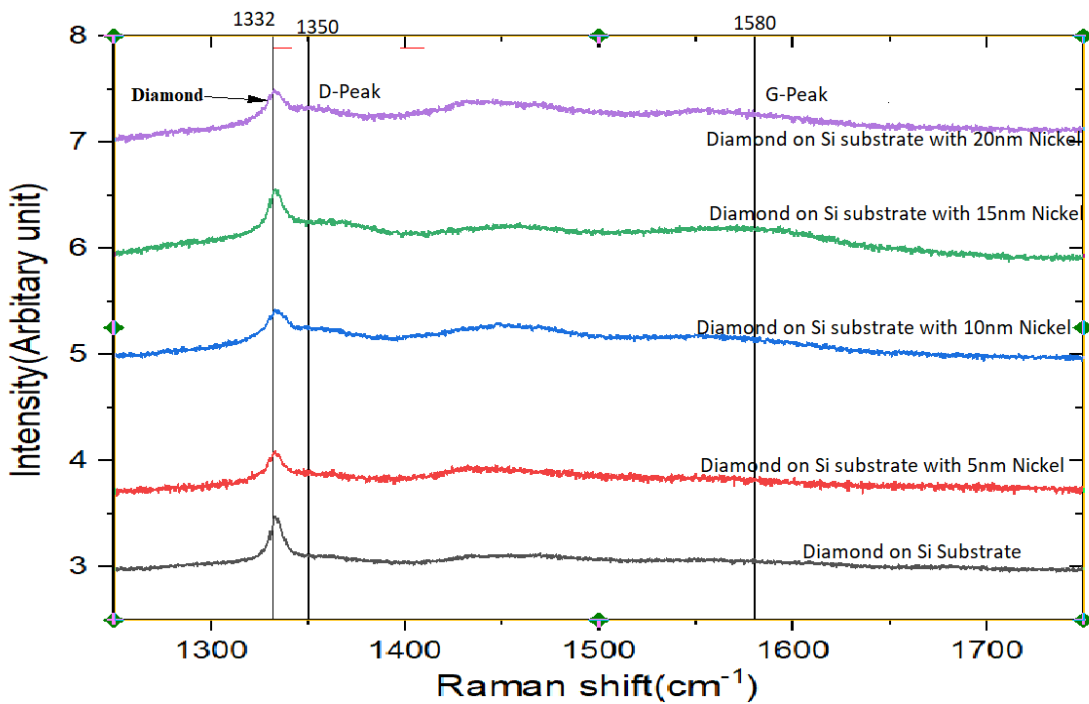
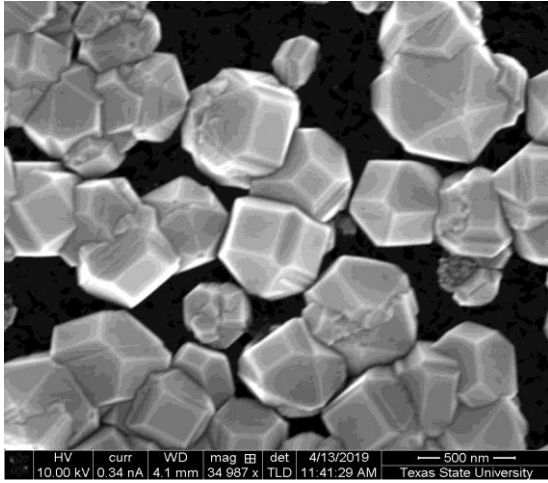
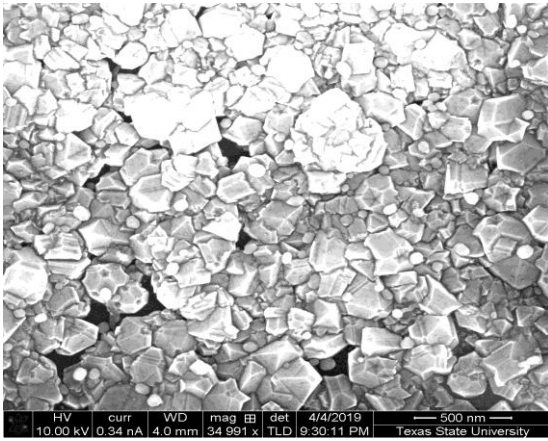
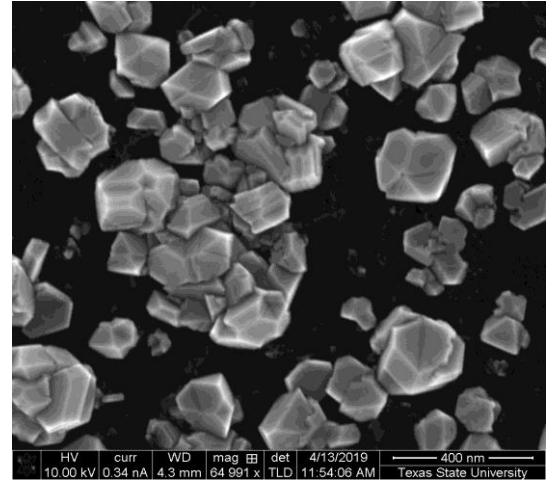


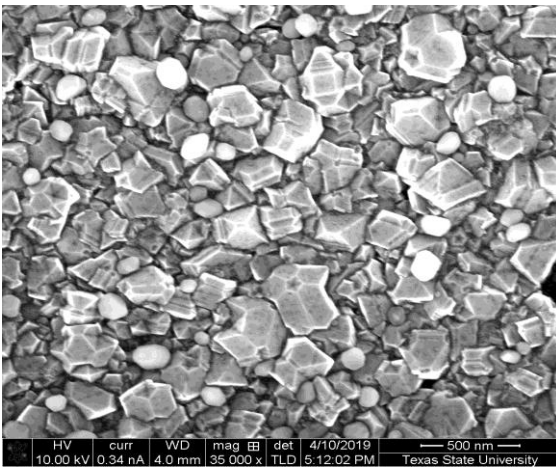
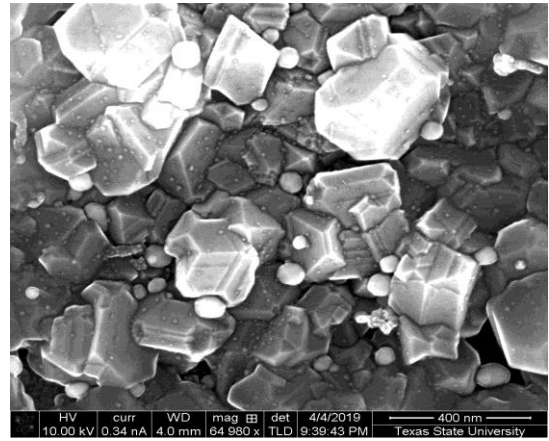
**Figure 44.** Raman spectra for the various samples in this study.



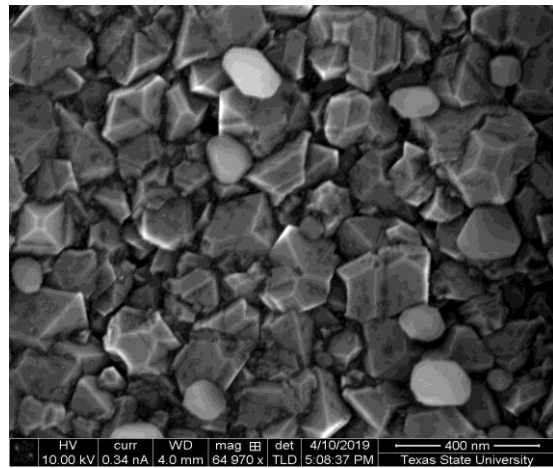
a)



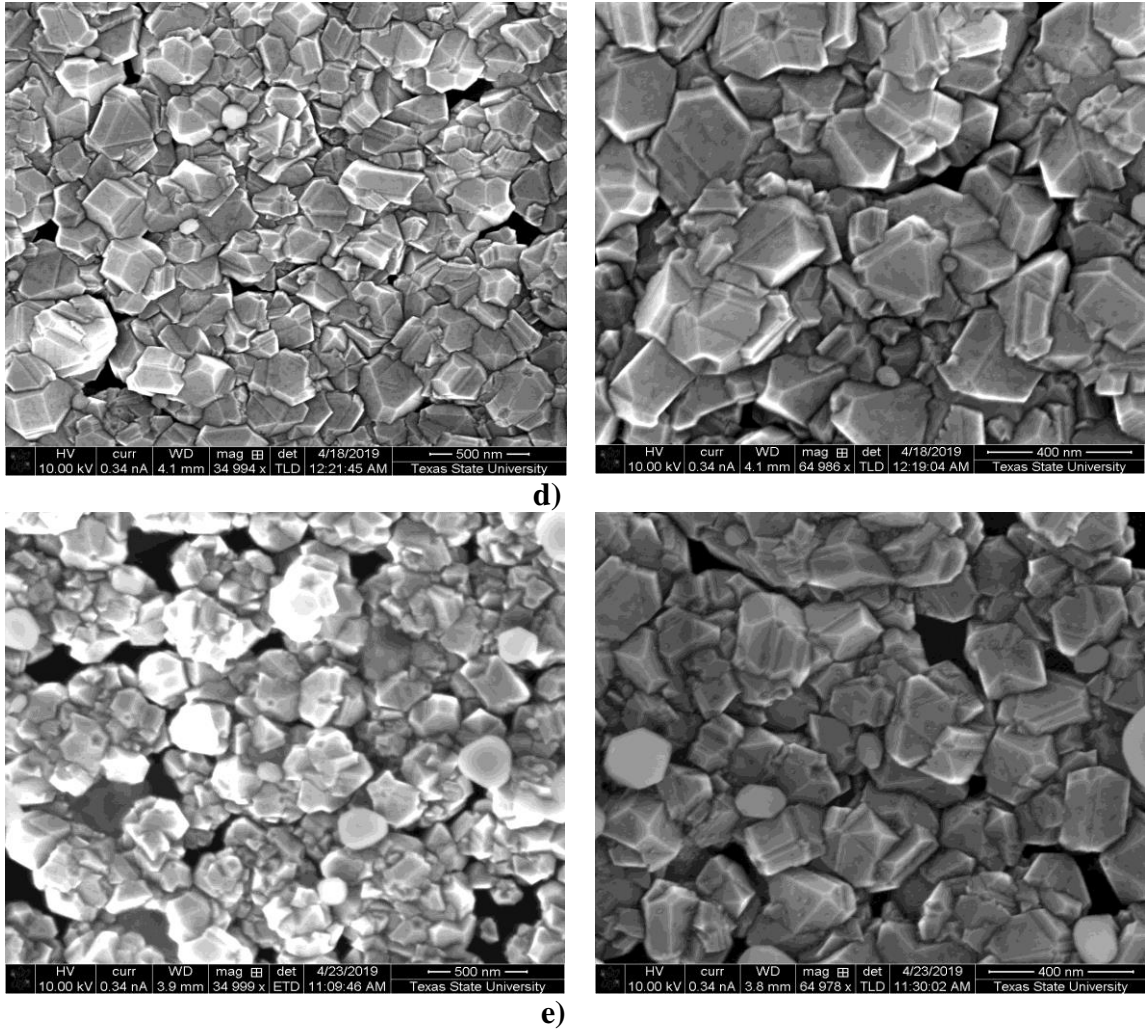
b)



c)



i) The figure (a)-(c) represents the diamond growth on bare silicon, 5nm Ni and 10 Ni respectively.

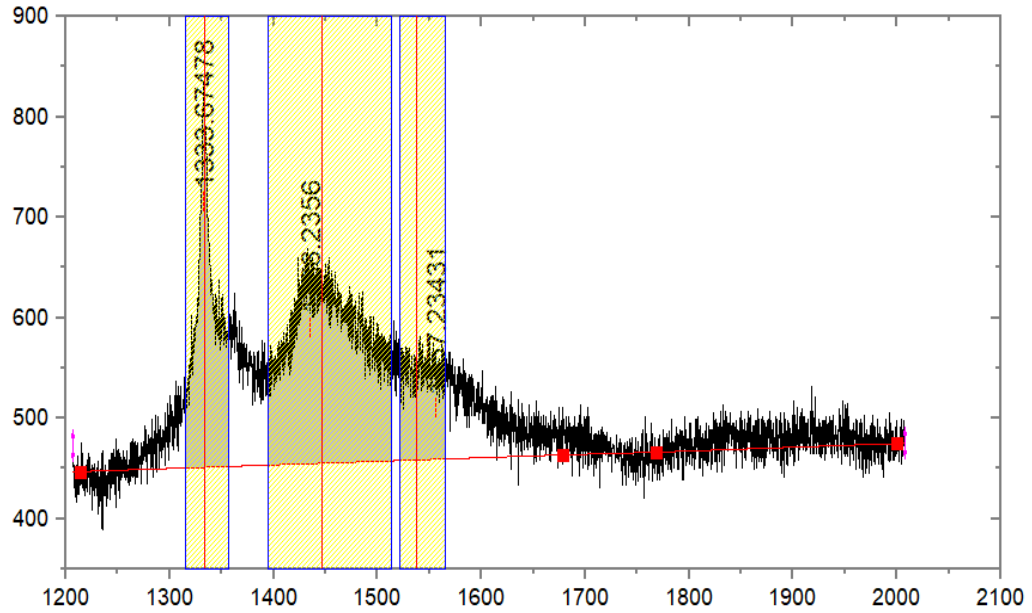


ii)The figure (d) and (e) represents the diamond growth on 15 nm and 20 nm Ni thin film on silicon substrate.

**Figure 45.** SEM images of diamond films grown on nickel modification layers; i)The figure shows SEM images of diamond films grown on, (a) Si substrate, (b) 5 nm Ni modification layer, (c) 10 nm Ni modification layer and ii)The figure shows diamond growth on (d) 15 nm Ni modification layer, and (e) 20 nm Ni modification layer.

The diamond peak is centered at  $1332\text{ cm}^{-1}$ , while the Raman peaks at  $1363\text{ cm}^{-1}$  and  $1567\text{ cm}^{-1}$  correspond to the D and G bands of graphite, respectively. The following two important trends can be concluded from the Raman spectra: 1) both blank Si substrate and Ni modified Si substrate exhibits similar carbon related Raman signals, and 2) Ni modified Si substrate has suppressed non-diamond peaks with larger FWHM,

which is representative of the larger diamond grains. These data indicate that the presence of the Ni modification layer improves the kinetics of diamond growth. Furthermore, the relative Raman intensity of the graphitic carbon peaks increases with increasing Ni layer thickness.



$$\text{Non diamond carbon contents} = (\text{peak 2} + \text{peak 3}) / (\text{peak 1} + \text{peak 2} + \text{peak 3}) = 0.74$$

Peaks	Area under the curve (Arb. Unit)
Peak 1	2580
Peak 2	7662
Peak 3	1003

**Figure 46.** Non-diamond composition from diamond Raman peaks; The area under the curve calculation for Raman peaks for diamond grown on 5nm nickel modification layer on a silicon substrate (Horizontal scale represent Raman shift in  $\text{cm}^{-1}$  and Vertical scale represent Intensity (arbitrary unit)).

The NDC content in the diamond films is calculated by a standard process [63,64] involving measuring the area under the curve of the diamond and NDC peaks from the Raman spectra, as represented in Figure 46. The area under the curve for both diamond and NDC peaks are determined by baseline curve fitting and the percentage of NDC is determined from the ratio of the  $sp^2$  bonded carbon to the sum of the areas for both  $sp^2$  and  $sp^3$  bonded carbon.

The variation of NDC and diamond film thickness with Ni modification layer thickness is shown in Figure 47. The data indicate that the percentage of NDC decreases with increasing Ni thickness, although the FWHM of the diamond increases with increasing Ni thickness as well, which signifies that the diamond grain size increases with the increasing Ni thickness.

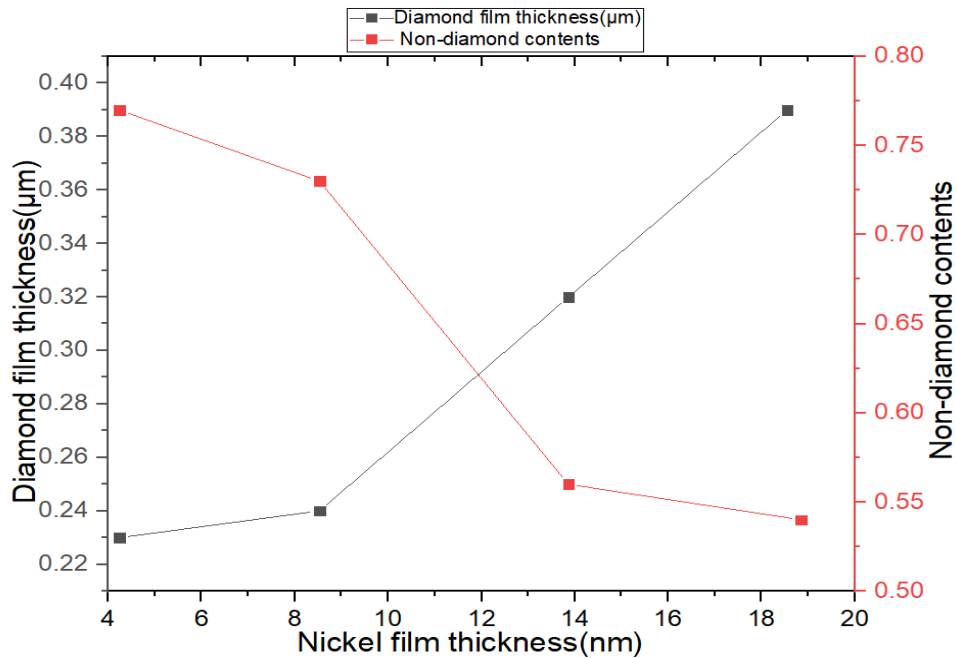


**Figure 47.** Variation of diamond thickness and NDC content with Ni modification layer thickness.

#### **4.2.4. Enhancement mechanism of diamond films grown on Ni modification layers**

The mechanism for enhancing preferential diamond orientation on Ni modified Si (111) is explained by the diffusion of Ni on silicon forming different phases of nickel silicide. Additionally, the atomic hydrogen may play a crucial role in the diffusion processes while the sample is subjected to the HFCVD environment. Introducing Ni modified layers to enhance diamond seeding and film growth seems contrary to some previously established conclusions [65] that Ni's high carbon solubility and its strong catalytic effect on hydrocarbon decomposition and subsequent graphite formation at low pressure would prevent diamond nucleation.

Graphitic interlayers will quickly form when Ni is placed in a methane-hydrogen atmosphere in HFCVD. On the one hand, when a Si substrate is modified with a thin Ni layer, Ni with empty 3d or 4s electronic states facilitates the rapid transformation of diamond seeds absorbed on the substrate into the graphitic layer [63]. It is believed that diamond seeds partially dissolve on these graphitic layers. Carbon reacts with the Ni lattice and forms a Ni-C eutectic phase. Both carbon and hydrogen dissolve into the Ni lattice but remains mainly on the surface region. Once the Ni-C-H intermediate state is formed, the locally supersaturated  $sp^3$  carbon acts as diamond nucleation centers on the Ni modified layers. The diamond growth follows a three-step process; first, two graphitic layers form, second, 5-6 additional graphitic layers very slowly grow, and finally, diamond growth starts [63]. The incumbent time for diamond growth from the graphitic interlayers is around 10 h, however, Ni modified layers significantly reduces such incumbent time to enhance the growth of diamond films [63,66]. Very thin Ni modified layers have abundant grains boundaries to provide channels for the diffusion of carbon

atoms. So, thin Ni modification layers do not require long times to compensate for the loss of carbon dissolved into the Ni. Once the critical thickness for carbon deposition is reached, the nucleation of diamond begins.

During the growth stage, the Ni modification plays a significant role in the nucleation of the diamond films. When a Si substrate with a Ni modification layer is placed in the HFCVD chamber, diffusion of Ni forms Ni-Si alloys. Due to the transformation of Ni into Ni-Si alloys, the carbon solubility decreases. The carbon dissolves into the Ni modification layer at the early nucleation stage, but then gradually out-diffuses where it acts as another carbon source for diamond growth, which will tend to form a large crystal diamond. Due to this, the NDC content decreases with increasing Ni thickness. The variation of diamond thickness and roughness measured by surface profilometry for the varied Ni thickness samples in this study is shown in Table 5.

**Table 5.** The diamond thickness and roughness measured by surface profilometer at a different position from the center.

Diamond grown on	Parameters	At X=15mm	At X=30mm	At X=45mm
Si substrate	Thickness( $\mu\text{m}$ )	(0.21 $\pm$ 0.03)	(0.17 $\pm$ 0.02)	(0.18 $\pm$ 0.01)
	Roughness(nm)	(45.43 $\pm$ 3.14)	(39.88 $\pm$ 2.67)	(43.66 $\pm$ 2.14)
5nm Ni layers on Si Substrate	Thickness( $\mu\text{m}$ )	(0.23 $\pm$ 0.02)	(0.21 $\pm$ 0.03)	(0.20 $\pm$ 0.03)
	Roughness(nm)	(38.37 $\pm$ 2.04)	(26.65 $\pm$ 2.05)	(26.49 $\pm$ 2.11)
10 nm Ni layers on Si Substrate	Thickness( $\mu\text{m}$ )	(0.24 $\pm$ 0.01)	(0.27 $\pm$ 0.02)	(0.26 $\pm$ 0.01)
	Roughness(nm)	(22.37 $\pm$ 1.64)	(23.50 $\pm$ 1.87)	(19.54 $\pm$ 2.12)
15nm Ni layers on Si Substrate	Thickness( $\mu\text{m}$ )	(0.32 $\pm$ 0.01)	(0.30 $\pm$ 0.01)	(0.28 $\pm$ 0.03)
	Roughness(nm)	(32.50 $\pm$ 1.24)	(39.27 $\pm$ 2.64)	(31.32 $\pm$ 1.44)
20nm Ni layers on Si Substrate	Thickness( $\mu\text{m}$ )	(0.39 $\pm$ 0.03)	(0.37 $\pm$ 0.02)	(0.33 $\pm$ 0.07)
	Roughness(nm)	(35.44 $\pm$ 1.88)	(28.91 $\pm$ 0.72)	(39.99 $\pm$ 1.62)

Diamond roughness typically depends upon the grain size which is also the case for this study. Grain size increases with increasing Ni modification layer thickness, which increases the surface roughness of the diamond films. Although the diamond roughness is slightly lower for the 10 nm Ni layer, as indicated in Figure 46, this may be due to the oriented growth of smooth diamond films with small grains size.

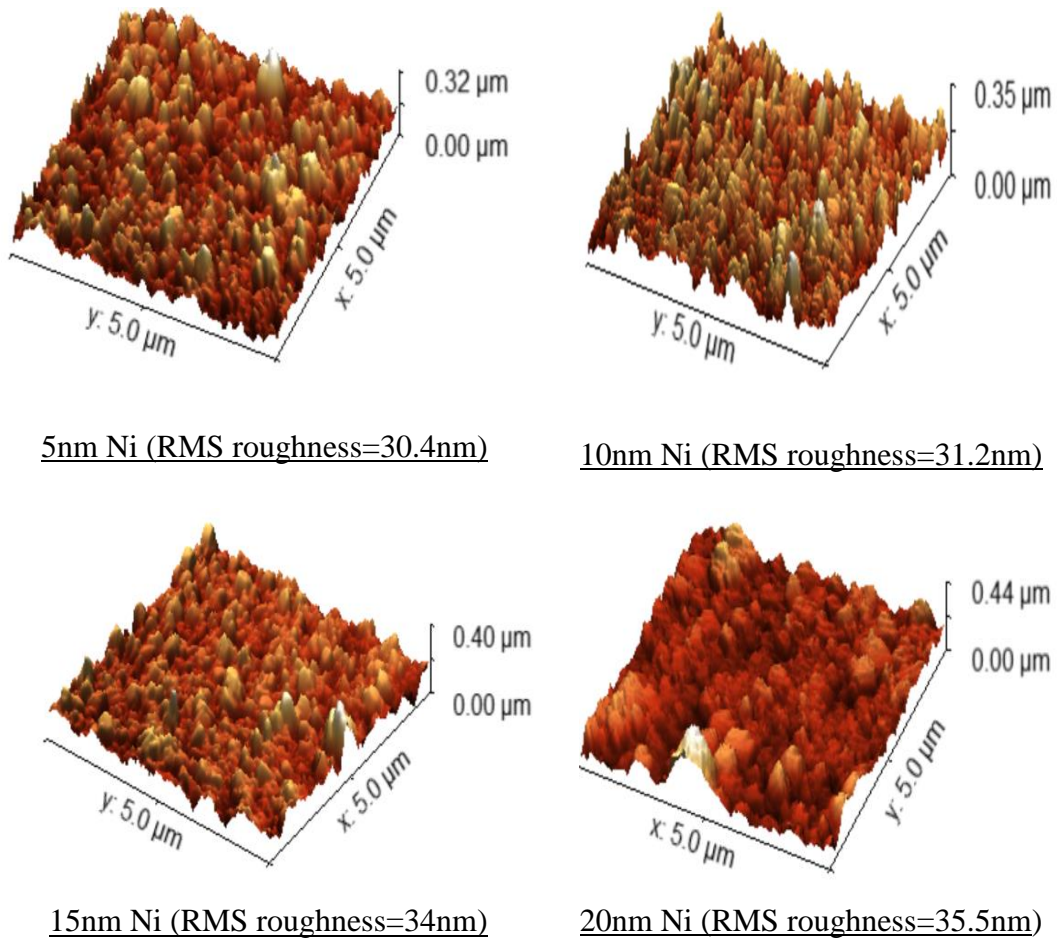


**Figure 48.** AFM images indicating surface morphologies of the diamond films grown with different Ni modification layers (wafer center).

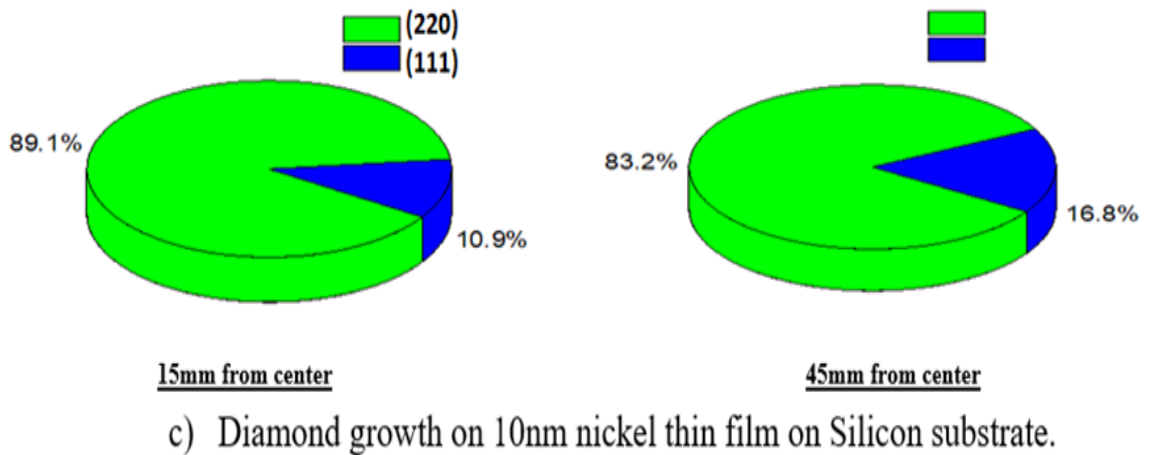
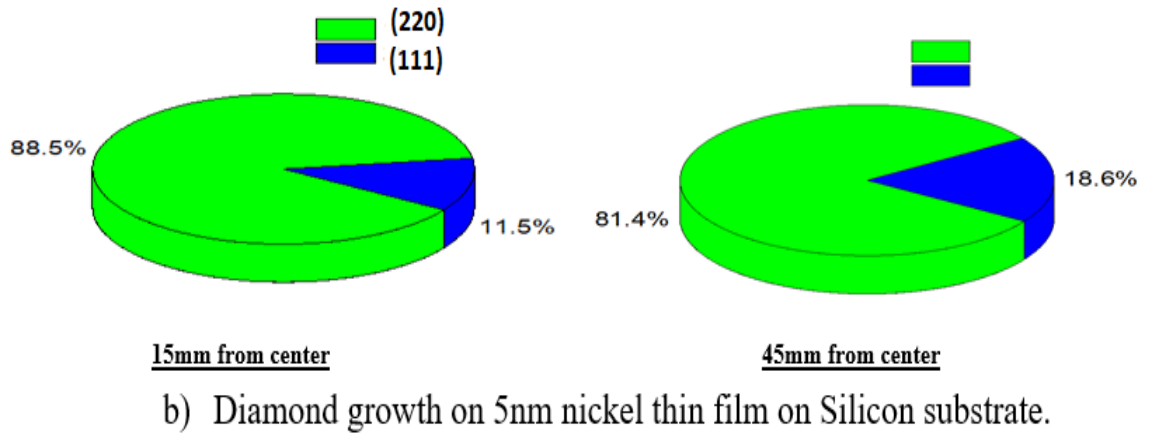
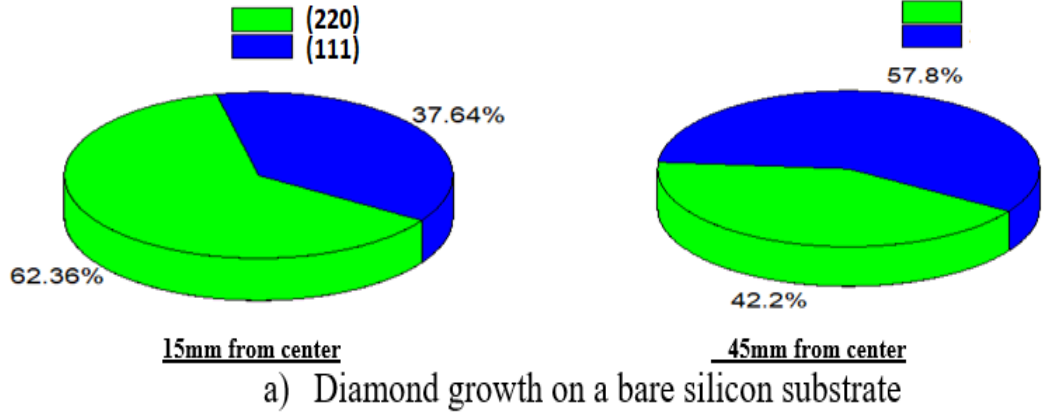
#### 4.2.5. Development of diamond texture

The Ni modification layer samples were characterized by medium resolution wide angle parallel beam XRD. The XRD scans show sharp (220) diamond peaks at 75.6° and weak (111) peaks at 43.9°. To characterize the diamond film texture, the observed intensities were compared to the spectrum from a randomly oriented diamond powder sample. The planar indices, 2-theta angle, d-spacing and expected random intensities of the diffracted beam for a randomly oriented diamond powder were taken from the American Society of Testing Materials (ASTM Card info 6-0675) and are given in Table 6.

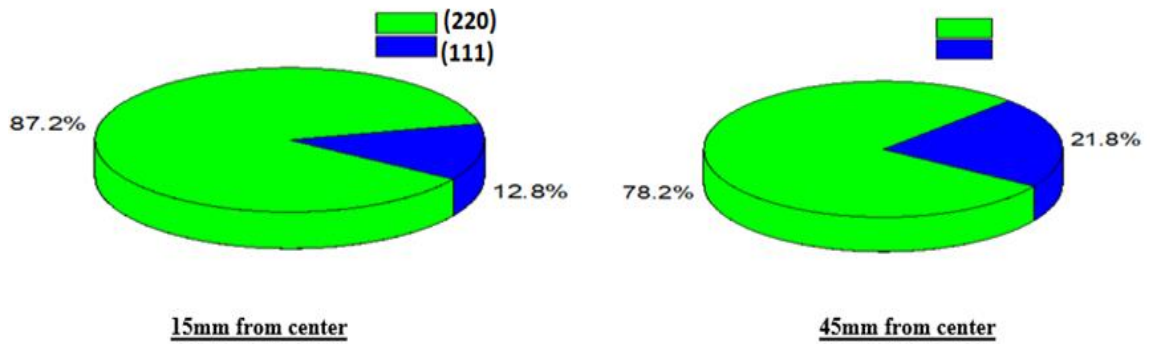
**Table 6.** Relative intensity of diffracted X-rays beams for random assembly of diamond crystals.

<b>h, k, l planer indices</b>	<b>2<math>\theta</math> angle(degree)</b>	<b>d-spacing (Angstrom)</b>	<b>Relative diffracted Intensity</b>
(111)	43.9	2.06	100
(220)	75.3	1.261	25
(311)	91.5	1.0754	16
(400)	119.5	0.8916	8
(331)	140.3	0.8182	16

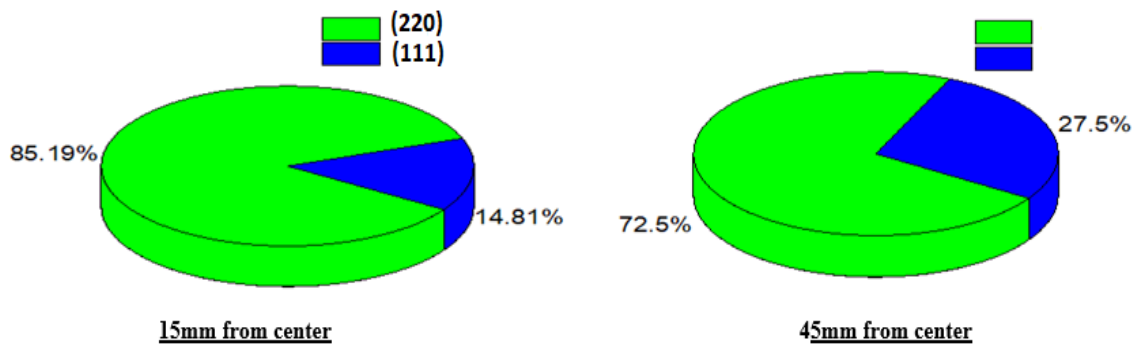
The area under the observed 2 $\theta$  peak positions (43.9° and 75.6° for diamond (111) and (220), respectively) were calculated for all samples. Each measured peak area was normalized by dividing by the relative diffracted intensity from the randomly oriented powder. Finally, the values are renormalized again by the total observable peak intensities to total 100%. These values are expressed graphically in Figure 49.



i) The figure (a)-(c) shows the crystal orientation distribution of diamond films grown on bare silicon, 5nm Ni modification layers and 10 nm Ni modifications layers respectively.



d) Diamond growth on 15nm nickel thin film on Silicon substrate.



e) Diamond growth on 20nm nickel thin film on Silicon substrate.

ii) The figure (d)-(e) shows the crystal distribution of diamond films grown on 15nm and 20 nm Ni modification layers respectively.

**Figure 49.** i) &ii), Crystal orientation distribution of diamond obtained from XRD for the samples grown with varied Ni modifications layer thickness.

From the analysis shown in Figure 49, the diamond film grown on the 10 nm Ni modified layer has the highest (220) oriented diamond at 89.1 %, as well as the lowest surface roughness. Generally, the diamond film texture decreases with increasing Ni modifications layer thickness. However, all Ni modified layer sample exhibits

substantially greater texture toward (220) compared to diamond grown without a Ni layer.

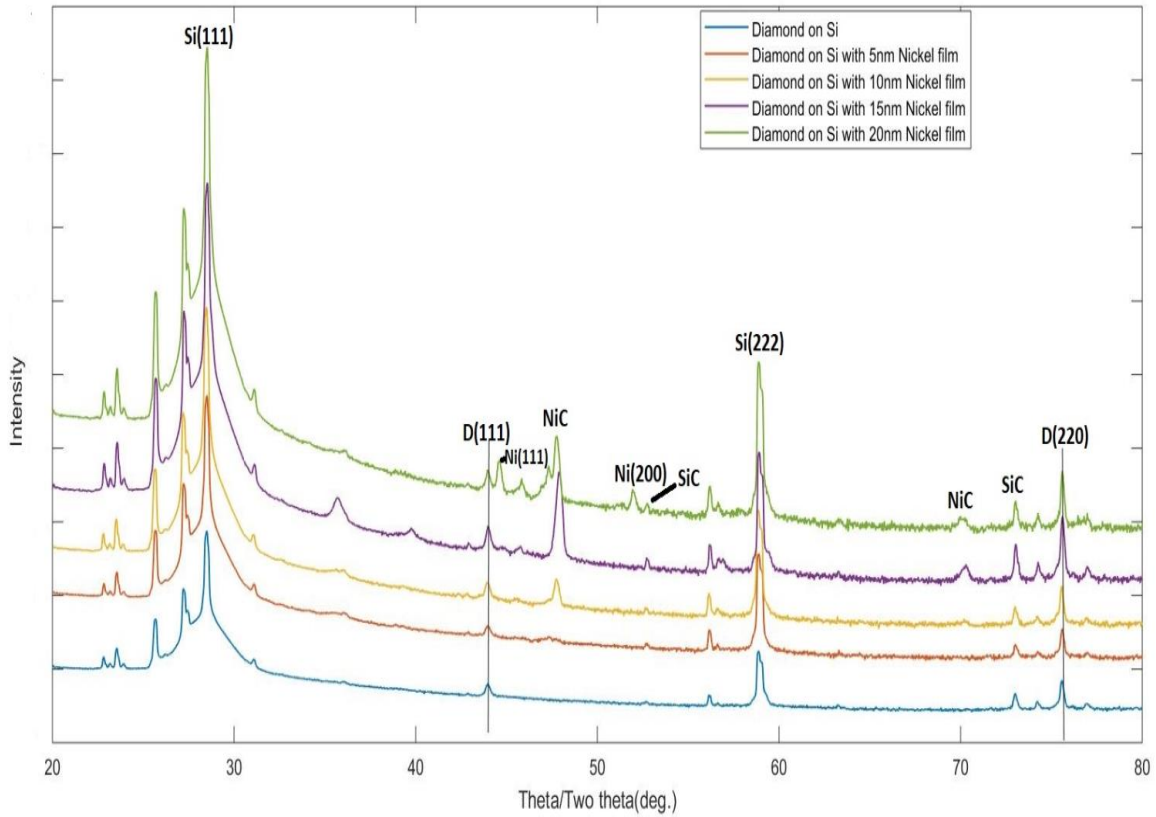


**Figure 50.** Medium resolution parallel beam XRD scans for diamond growth on different Ni modification layer thickness.

### Reasons for diamond films texture

During diamond growth on Ni modified silicon (111), the diamond film grows prismatically on graphitic planes by distorting the carbon angles and bonds starting at the edges and corners of the graphitic layer. This may be thought of as pseudo-heteroepitaxial growth of diamond on the nickel carbide intermediate layer, which forms when Ni modified Si is subjected to the HFCVD environment, discussed previously.

Since the thin Ni film is preferentially oriented along the (220) direction (see Figure 33) with small grain boundaries, diamond seeds that are located at the corners and edges of the graphitic planes can orient along with the Ni film texture resulting in the (220) oriented diamond film. The diamond seeds attempt to attain minimum surface energies and orient along the (220) direction, then the resultant diamond film grows along the (220) direction. The diamond texture decreases with increasing Ni films thickness due to a decrease in grain boundary density. The XRD scans for diamond grow on different thickness Ni modified layer are shown in Figure 50, which shows that most of the diamond nuclei orient along the (220) direction resulting in the film getting preferentially oriented along that direction. The diamond films were preferential oriented for the very thin nickel thickness and the degree of texture decreases with increasing thickness of the nickel modification layers.

Another way to explain the oriented diamond film is by the Frank Van der Merve growth mechanism. When the Ni modified Si substrate is placed in the HFCVD chamber with hydrogen + methane atmosphere, both carbon and hydrogen dissolve into the Ni lattice and Ni + C (and hydrogen) eutectic phases are formed, which has a NaCl type crystal structure [65]. The diamond seeds are expected to partially dissolve in the eutectic nickel carbides phases and remain mostly at the grain boundaries. The undissolved diamond seeds at the NiC phases starts to grow from the grain boundaries. The carbon and hydrogen that remain on the surface provides a pathway to diamond deposition. Since NiC and diamond have a close lattice constant ( $a_{\text{NiC}} = 3.52 \text{ \AA}$  &  $a_{\text{diamond}} = 3.57 \text{ \AA}$ ), the diamond film may grow on thin layers of NiC epitaxially resulting in diamond grains oriented along (220) with smooth films

## V. CONCLUSIONS

### 5.1. Diamond growth on annealed seeded wafers with nickel layers

High-quality diamond films with large grains, low surface roughness and low NDC (less than 15%) is achieved by a multistep deposition technique that includes annealing the diamond seeded wafer at different temperatures in the presence of N<sub>2</sub> gas. Highly oriented (111) diamond nuclei, corresponding to the substrate orientation, are achieved by annealing. The oriented diamond nuclei are due to the orientation of diamond seeds along the substrate orientation, explained by partial dissolution of diamond nuclei in nickel silicide nanodots. The reorientation of diamond seeds is due to the stress induced between the diamond nuclei and nickel silicide nanodots formed by annealing. Due to the formation of nickel carbide phases during diamond growth, well faceted diamond is formed with minimum non-diamond carbon (NDC).

### 5.2. Diamond growth on Si wafer with nickel modification layers

#### 5.2.1. High Growth rate /Nucleation

The fast nucleation kinetics on a Ni modified surface yields a large diamond nucleation density resulting in the formation of highly coalesced diamond films within 3 h of diamond deposition by HFCVD. The thickness of the diamond films increases with increasing modified Ni layer thickness. The reason for fast nucleation is the formation of graphitic layers that act as an intermediate layer and an additional supply of carbon.

### **5.2.2. High-quality diamond film and crystallinity**

Due to the diffusion of Ni in Si to form various Ni-Si alloys, the carbon solubility in the Ni modification layers gradually decreases over time allowing and dissolved carbon from the early stage of nucleation to out-diffuse, later. This provides another carbon source for the diamond crystal growth resulting in the formation of high-quality diamond films.

### **5.2.3. Oriented diamond films along (220)**

When the Ni modified Si substrate is exposed to the HFCVD environment with hydrogen and methane, both carbon and hydrogen dissolve into the Ni lattice and a Ni-C (and hydrogen) eutectic phase are formed which has a NaCl crystal structure. The carbon and hydrogen that remain on the surface provides a pathway for diamond deposition. Diamond layers grown a top of NiC films (which has a close lattice parameter as diamond) follow the Frank Van der Merve growth mechanism resulting in oriented films that correspond to the NiC film texture.

## VI. FUTURE WORK

Two main directions of future works are envisioned. First is the growth of diamond films on annealed nickel films of various thickness by different annealing processes, such as rapid thermal processing (RTP). One challenge for the conventional annealing process conducted in this research was the control of the accumulating heat at the surface of the nanodots. Thus, it is anticipated that better control over the dissolution of diamond seeds on Ni nanodots can be achieved by RTP. Since Ni nanodot density is maximized with thin Ni films, RTP may further aid in the equal distribution of diamond seeds resulting in faster coalescence of the diamond film. Highly preferentially crystalline oriented, high-quality diamond films, due to the highly oriented diamond nuclei, can be expected with this technique.

Second is investigating further diamond texture modification by additional diamond growth on the samples with Ni modification layers which were grown 3 h, previously. Additionally, published research has discussed the effect of HFCVD growth parameters such as methane concentration, deposition temperature, etc., on preferentially oriented diamond growth. Since samples with highly coalesced diamond films oriented along the (220) direction can be produced with the approach investigated in the present research, we also investigate additional parameters, such as methane concentration, to potentially realize further improved diamond quality and preferred orientation. Additionally, other characterization techniques, such as x-ray pole figure analysis, can be employed for the texture analysis. Finally, a key enabling feature of oriented diamond is improved phonon transport. Thus, thermal conductivity measurements are of significant interest.

## APPENDIX SECTION

The purpose of this section is to supply supplementary information about measurement and equipment specifications for the growth and characterization of Ni and diamond films on silicon. This material is supplied to give the necessary details required to reproduce the reported methods and results.

### **E-beam deposition by Angstrom engineering Evo Vac**

Angstrom Engineering Evo Vac system was used for the deposition of Ni. The deposition conditions include a chamber pressure up to  $3.63 \times 10^{-8}$  Torr, load lock pressure  $1.22 \times 10^{-7}$  Torr and cryo heat temperature at 10 K. The deposition rate was maintained at  $0.5 \text{ \AA/s}$  for all samples, and the position of the sample stage was maintained at 47 mm.

### **Diamond growth from HFCVD**

The Texas State Crystallume EC-001T CVD Diamond Deposition System was used to deposit all diamond films. The deposition conditions include 1.5% methane concentration with 2 LPM  $\text{H}_2$ , and 3 sccm  $\text{O}_2$ . The growth time was 3-9 h. The chamber pressure was kept at 20.8 Torr, and tungsten filament wire was changed during each deposition to protect the sample from contamination, as per standard procedure. The distance between the substrate and wire was 6 mm.

### **Diamond blanket seeding**

Nano diamond seeding was conducted on the Laurell EDC Spin Coater in the Texas State cleanroom. The seed solution was made by mixing 3 ml of S1813 photoresist, 1 ml of DMSO and 1 ml of diamond seed, per our research group's standard procedure. Before processing, the uniformity of the photoresist was tested by using 3 ml of S1813 photoresist and 2 ml of DMSO and evaluated with the Film metrics System by measuring from 300-1200 nm. The run parameters for the spin coater were 2500 rpm with 1000 rpm acceleration for 25 sec. Before seeding, the solution was heated for 3 min, and the wafer for 25 sec, at 115 °C. After seeding, the substrate was heated for 20 sec to set the photoresist. The seeding was conducted at the standard cleanroom temperature and humidity.

### **Three-zone tube furnaces**

The Lindberg Three Zone tube furnace was used for wafer annealing in the presence of nitrogen gas. The nitrogen flow rate was established with 20 psi pressure. The annealing temperature was set by the three temperature controllers (TCs). The desired temperature was set by the middle TC, while the side TC was set 5% off of the middle.

### **Atomic Force Microscopy**

The Bruker Dimension ICON system was used for all AFM measurements utilizing tapping mode at room temperature. The AFM tip was HQ:NSC14Al/BS. The tip has an average operating frequency of 160 kHz with an average force constant of 5 N/m. The amplitude setpoint was set between 10-15 nm, depending upon the image resolution.

### **Stylus Profilometer**

Bruker DekTak XT was used with a 2  $\mu\text{m}$  stylus tip radius with 3 mg tip force. The scan length for all measurements was 500 nm. Thickness and roughness measurements were taken at three different wafer positions; 15 mm, 30 mm, and 45 mm from the center.

### **Scanning Electron Microscopy and Energy Dispersive X-ray spectroscopy (EDS)**

The FEI Helios Nano lab 400 dual beam system was used. The accelerating voltage and current were 10 kV and 0.34 nA, respectively. Scans were taken at different wafer positions; 15mm, 30mm, and 45mm from the center of the wafer. Both Field free mode and Immersion mode was used to take images of the sample surface.

### **X-ray Diffraction Crystallography**

The Rigaku Smart Lab X-ray Diffractometer was utilized for all XRD measurements. Standard Bragg Brentano  $\theta/2\theta$  measurements were taken in Medium Resolution parallel beam mode. The voltage and current for the x-ray source were fixed at 40 kV and 44 mA, respectively. The source-side length limiting slit was 7 mm, and the detector side monochromator was 5° soller slit. The x-y stage was used to scan different wafer positions at 15 mm, 30 mm, and 45 mm from the center. The  $\theta/2\theta$  angle was fixed from 20-100 °, and the scan speed was 3 deg./min with a step size of 0.01 °.

### **Ellipsometer**

The J.A. Woollam Ellipsometer was used to measure the Ni film thickness. Two incidence angles were used; 55 and 65 °. The Cauchy simulation model for transparent films on silicon was employed. The wavelength was 300-1200 nm.

### **Raman Spectroscopy**

Horiba Lab RAM HR Raman spectroscopy was used for the chemical analysis of the diamond film. The 532 nm solid-state laser was used to measure the Raman shift of the diamond films from 450-2000  $\text{cm}^{-1}$ . The acquisition time was set to 8 sec, and a 10 % filter was used.

## REFERENCES

- [1] J. J. Gracio, Q. H. Fan, and J. C. Madaleno, *J. Phys. D. Appl. Phys.* **43**, (2010).
- [2] S. Koizumi, C. Nebel, and M. Nesladek, *Physics and Applications of CVD Diamond* (WILEY-VCH Verlag GmbH & Co. KGaA, 2008).
- [3] M. N. R. Ashfold, P. W. May, C. A. Rego, and N. M. Everitt, *Chem. Soc. Rev.* **23**, 21 (1994).
- [4] K. Kobashi, *Orient D and Films* (ELSEVIER ltd, The Boulevard, Langford Kidlington, Oxford OX5 1GB, UK, 2005).
- [5] P. C. Yang, W. Zhu, and J. T. Glass, **7919**, 1773 (2017).
- [6] H. M. Strong and R. E. Hanneman, *J. Chem. Phys.* **46**, 3668 (1967).
- [7] R. B. Heimann, S. E. Evsyukov, and Y. Koga, *Carbon N. Y.* **35**, 1654 (1997).
- [8] P. W. May, *Philos. Trans. R. Soc. A Math. Phys. Eng. Sci.* **358**, 473 (2000).
- [9] S. T. Lee, Z. Lin, and X. Jiang, *Mater. Sci. Eng. R Reports* **25**, 123 (1999).
- [10] V. Kunderát, *Ast. Univ.* 177 (2015).
- [11] M. Amaral, P. S. Gomes, M. A. Lopes, J. D. Santos, R. F. Silva, and M. H. Fernandes, *Acta Biomater.* **5**, 755 (2009).
- [12] S. Mitura, A. Mitura, P. Niedzielski, and P. Couvrat, *Chaos, Solitons and Fractals* **10**, 2165 (1999).
- [13] R. a. Gudmundsen and R. P. Ruth, *Proc. IEEE* **6**, 376 (1971).
- [14] J. Hoebert, P. Souverein, A. Mantel-Teeuwisse, H. Leufkens, and L. Van Dijk, *Huisarts Wet.* **55**, 286 (2012).
- [15] M. G. Mykoniatis, *Immobilization of Native and Denatured DNA on Sephadex G200* (1985).

- [16] X. Kuang, J. Tian, H. Guo, Y. Hou, H. Zhang, and T. Liu, *Mater. Tehnol.* **52**, 119 (2018).
- [17] P. Smereka, X. Li, G. Russo, and D. J. Srolovitz, *Acta Mater.* **53**, 1191 (2005).
- [18] A. Engineering and C. Kitchener, *Ontario*, **91**, 399 (2017).
- [19] Crystallume and Crystallume.com, 2 (2008).
- [20] V. Joost, *thin film mechanics*, 26 (2004).
- [21] M. D. Drory and J. W. Hutchinson, *Proc. R. Soc. A Math. Phys. Eng. Sci.* **452**, 2319 (1996).
- [22] M. J. Kim, J. S. Lee, S. K. Kim, G. Y. Yeom, J. B. Yoo, and C. Y. Park, *Thin Solid Films* **475**, 41 (2005).
- [23] J. Kim, W. Jang, J. Park, H. Jeon, H. Kim, J. Yuh, and H. Jeon, *J. Korean Phys. Soc.* **66**, 821 (2015).
- [24] C. B.D and Stock Stuart, in *Elem. X-Ray Diffr.*, 3rd ed. (Prentice Hall, 2001), p. 33.
- [25] M. Yeadon, R. Nath, C. B. Boothroyd, and D. Z. Chi, *Des. Nat.* **6**, (2004).
- [26] A. T. Submitted, F. O. R. The, D. Of, and M. Of, *Direct* (2004).
- [27] T. O. H. Iwai, *Nickel Silicide formation for high resistive nickel phases*, 1 (2002).
- [28] B. Hettich and G. Materialforschung, *J. Adv. Mater.* **3**, 8 (1991).
- [29] P. Morin, T. H. Applebaum, R. Bowman, Y. Zhao, C. Multilingual, W. Recog, P. Morin, B. A. Hanson, T. H. Applebaum, P. Examiner, and V. B. Chawan, **1**, (2002).
- [30] H. Lee, S. D. Lopatin, and S. S. Wong, *Proc. IEEE 2000 Int. Interconnect Technol. Conf. IITC 2000* **3796**, 114 (2000).

- [31] T. Scherban, P. S. Ho, D. Gan, J. Maiz, R. Huang, J. Leu, and Y. Pang, *J. Mater. Res.* **21**, 1512 (2006).
- [32] J. M. Zhang, K. W. Xu, and V. Ji, *Appl. Surf. Sci.* **180**, 1 (2001).
- [33] D. B. Bogy, Z. Feng, J. W. Ager, Z. Wang, A. Anders, K. Komvopoulos, S. Anders, and I. G. Brown, *J. Appl. Phys.* **79**, 485 (2002).
- [34] H. Liu and D. S. Dandy, *Diam. Relat. Mater.* **4**, 1173 (1995).
- [35] H. Ye, C. Q. Sun, P. Hing, H. Xie, S. Zhang, and J. Wei, *Surf. Coatings Technol.* **123**, 129 (2000).
- [36] A. Vul, M. Baidakova, and A. Dideikin, *Nanomater. Handbook*, Second Ed. **20**, 351 (2017).
- [37] P. A. Nistor and P. W. May, *J. R. Soc. Interface* **14**, (2017).
- [38] H. Buchkremer-Hermanns, H. Ren, and H. Weiß, *Diam. Relat. Mater.* **5**, 312 (2002).
- [39] A. J. Neves, M. H. Nazaré, J. C. Lopes, and H. Kanda, *Phys. B Condens. Matter* **273–274**, 636 (1999).
- [40] A. Vanhulsel, J. P. Celis, E. Dekempeneer, J. Meneve, J. Smeets, and K. Vercammen, *Diam. Relat. Mater.* **8**, 1193 (1999).
- [41] T. Liu, D. Raabe, and W. M. Mao, *Signal, Image Video Process.* **4**, 1 (2010).
- [42] S. Y. Qin, S. S. Xu, R. X. Zhuo, and X. Z. Zhang, *Langmuir* **28**, 2083 (2012).
- [43] T. Liu, D. Raabe, W. Mao, and S. Zaefferer, *Adv. Funct. Mater.* **19**, 3880 (2009).
- [44] D. Meakin, J. Stoemenos, P. Migliorato, and N. A. Economou, *J. Appl. Phys.* **61**, 5031 (1987).

- [45] E. Titus, D. S. Misra, M. K. Singh, P. K. Tyagi, A. Misra, F. Le Normand, J. Gracio, and N. Ali, *J. Mater. Res.* **19**, 3206 (2004).
- [46] A. R. Badzian and T. Badzian, *Surf. Coatings Technol.* **36**, 283 (1988).
- [47] G. J. Peter, H. John, and B. Richard, (Taylor & Francis , New Fetter lane, London EC4P 4EE, London and New York, 2001).
- [48] S. N. Magonov and D. H. Reneker, *Annu. Rev. Mater. Sci.* **27**, 175 (2002).
- [49] R. Gottimukkala, <http://scholarcommons.usf.edu/etd/2904>. 1,80 (2005).
- [50] T. Itoh, A. Sujith, and Y. Ozaki, *Front. Mol. Spectrosc.* 289 (2009).
- [51] R. Spectroscopy and F. Nanotubes, *R. Soc.* **362**, 2537 (2018).
- [52] A. C. Ferrari and J. Robertson, *Phys. Rev. B - Condens. Matter Mater. Phys.* **64**, 1 (2001).
- [53] S. M. Huang, Z. Sun, Y. F. Lu, and M. H. Hong, *Surf. Coatings Technol.* **151–152**, 263 (2002).
- [54] A. R.M and Bashara N.M, (North-Holland Publishing Company-Amsterdam-New York-Oxford, 1977).
- [55] N. J. Podraza and G. E. Jellison, *Encycl. Spectrosc. Spectrom.* 482 (2016).
- [56] E. Morrison, *Nanotechnology* **7**, 37 (1996).
- [57] J. C. García, A. Sanz Lobera, P. Maresca, T. F. Pareja, and C. Wang, *Materials (Basel)*. **11**, 1484 (2018).
- [58] N. Ahmad, J. Stokes, N. A. Fox, M. Teng, and M. J. Cryan, *Nano Energy* **1**, 777 (2012).
- [59] Y. S. Jang and J. H. Yoon, *IEEE Trans. Electron Devices* **56**, 3236 (2009).
- [60] D. Connétable and O. Thomas, *J. Alloys Compd.* **509**, 2639 (2011).
- [61] T. Inada, S. Tohyama, Y. Funaki, K. Itoh, and E. Nisi, **56**, 171 (2019).

- [62] C. Torregiani, J. D'Haen, K. Opsomer, M. J. Van Dal, P. van Houtte, and K. Maex, *Mater. Sci. Forum* **495–497**, 1431 (2009).
- [63] X. Z. Liu, Q. P. Wei, H. Zhai, and Z. M. Yu, *Trans. Nonferrous Met. Soc. China* (English Ed. **23**, 667 (2013)).
- [64] A. Hu and W. W. Duley, *Chem. Phys. Lett.* **450**, 375 (2008).
- [65] A. Badzian and T. Badzian, *MRS Proc.* **250**, 339 (2011).
- [66] P. C. Yang, R. Schlessler, C. A. Wolden, W. Liu, R. F. Davis, Z. Sitar, and J. T. Prater, *Appl. Phys. Lett.* **70**, 2960 (1997).